TOPICAL REVIEW • OPEN ACCESS

Matter under extreme conditions experiments at the Linac Coherent Light Source

To cite this article: S H Glenzer *et al* 2016 *J. Phys. B: At. Mol. Opt. Phys.* **49** 092001

OPEN ACCESS
IOP Publishing
Journal of Physics B: Atomic, Molecular and Optical Physics
J. Phys. B: At. Mol. Opt. Phys. **49** (2016) 092001 (26pp)
doi:10.1088/0953-4075/49/9/092001

Topical Review

Matter under extreme conditions experiments at the Linac Coherent Light Source

S H Glenzer[1], L B Fletcher[1], E Galtier[1], B Nagler[1], R Alonso-Mori[1], B Barbrel[2,3], S B Brown[1], D A Chapman[4], Z Chen[1], C B Curry[1], F Fiuza[1], E Gamboa[1], M Gauthier[1], D O Gericke[5], A Gleason[6], S Goede[1], E Granados[1], P Heimann[1], J Kim[1], D Kraus[3], M J MacDonald[1,7], A J Mackinnon[1], R Mishra[1], A Ravasio[8], C Roedel[1], P Sperling[1], W Schumaker[1], Y Y Tsui[9], J Vorberger[10], U Zastrau[11], A Fry[1], W E White[1], J B Hasting[1] and H J Lee[1]

[1] SLAC National Accelerator Laboratory, 2575 Sand Hill Road, MS 19, Menlo Park, CA 94025, USA
[2] Université de Bordeaux-CNRS-CEA, Centre Lasers Intenses et Applications (CELIA), Talence, F-33405, France
[3] Physics Department, University of California Berkeley, Berkeley, CA 94709, USA
[4] AWE plc, Aldermaston, Reading RG7 4PR, UK
[5] Centre for Fusion, Space and Astrophysics, Department of Physics, University of Warwick, Coventry CV4 7AL, UK
[6] Los AlamosNational Laboratory, Los Alamos, NM 87545, USA
[7] University of Michigan, Ann Arbor, MI 48109, USA
[8] LULI, École Polytechnique F-91128 Palaiseau Cedex, France
[9] Department of Electrical and Computer Engineering, University of Alberta, Edmonton, Alberta, Canada
[10] Max Planck Institute for the Physics of Complex Systems, Noethnitzer Strasse 38, D-01187 Dresden, Germany
[11] European XFEL GmbH, Albert-Einstein-Ring 19, D-22761 Hamburg, Germany

E-mail: glenzer@slac.stanford.edu

Received 27 August 2015, revised 3 December 2015
Accepted for publication 20 January 2016
Published 22 April 2016

Abstract

The matter in extreme conditions end station at the Linac Coherent Light Source (LCLS) is a new tool enabling accurate pump–probe measurements for studying the physical properties of matter in the high-energy density (HED) physics regime. This instrument combines the world's brightest x-ray source, the LCLS x-ray beam, with high-power lasers consisting of two nanosecond Nd:glass laser beams and one short-pulse Ti:sapphire laser. These lasers produce short-lived states of matter with high pressures, high temperatures or high densities with properties that are important for applications in nuclear fusion research, laboratory astrophysics and the development of intense radiation sources. In the first experiments, we have performed highly accurate x-ray diffraction and x-ray Thomson scattering measurements on shock-compressed matter resolving the transition from compressed solid matter to a co-existence regime and into the warm dense matter state. These complex charged-particle systems are

dominated by strong correlations and quantum effects. They exist in planetary interiors and laboratory experiments, e.g., during high-power laser interactions with solids or the compression phase of inertial confinement fusion implosions. Applying record peak brightness x-rays resolves the ionic interactions at atomic (Ångstrom) scale lengths and measure the static structure factor, which is a key quantity for determining equation of state data and important transport coefficients. Simultaneously, spectrally resolved measurements of plasmon features provide dynamic structure factor information that yield temperature and density with unprecedented precision at micron-scale resolution in dynamic compression experiments. These studies have demonstrated our ability to measure fundamental thermodynamic properties that determine the state of matter in the HED physics regime.

Keywords: high-energy density physics, free electron x-ray laser, x-ray scattering, warm dense matter, dynamically compressed matter

(Some figures may appear in colour only in the online journal)

1. Introduction

Matter in extreme conditions (MEC) is central to scientific research aimed at demonstrating nuclear fusion in the laboratory [1–5], for developing intense radiation sources with unique properties [6–11], and to many fundamental physics processes in astrophysics [12–18]. The capabilities of the linac coherent light source (LCLS) allow unprecedented explorations in this area of research enabling ultrafast probing with high-repetition rates and high x-ray photon energies [19]. It is particularly suited for a class of experiments that produces short-lived states of matter with extreme conditions using intense high-power laser beams where penetrating high-peak brightness x-rays resolve the dynamic evolution of the target [20]. The x-rays visualize structural changes and determine the physical properties with spectrally resolved x-ray scattering [21, 22], x-ray imaging [23] and x-ray diffraction [22–25]. High repetition rates allow averaging and summation over many experiments to produce unprecedented data quality with large signal-to-noise ratios and high confidence in the results [21]. For this purpose, the LCLS x-ray beam has recently been combined with high-power lasers and a suite of optical and x-ray diagnostics at the MEC instrument located in the far experimental hall (FEH) of LCLS.

An areal view of LCLS and the location of the near and FEH are shown in figure 1. LCLS delivers approximately 10^{11}–10^{12} x-ray photons in a micron-scale focal spot and when operated in a seeded mode [26] allows measurements with high spectral resolution of $\Delta E/E = 10^{-4}$, high wavenumber resolution of $\Delta k/k = 10^{-2}$, and high temporal resolution of 20–50 fs. The MEC instrument is equipped with one ultra-short pulse laser and two nanosecond laser beams that drive the material into extreme matter conditions, accessing a large phase space of high energy density (HED) physics coupled with the unique LCLS x-ray beam. At present, temperatures of 100 eV at solid density or a few eV at 3 times solid density have been reported [21, 27]. Recently, high-power ultra-short pulse laser–gas interaction experiments [28] have begun exploring much higher temperatures at sub-atmospheric target densities.

Figure 2 shows the temperature–density parameter space that is currently accessible for ultrafast high-resolution pump–probe studies together with the expected increase after upgrading the short pulse laser to 100–200 TW peak power. Importantly, the parameter space overlaps with areas in phase space where the conditions access important physics areas and processes. For example at low temperatures, conditions can be produced that are found in giant planets, planetary interiors, brown dwarfs or meteor impacts. Both isochoric heating using free electron laser radiation [21, 29–32] or a high-power laser-produced radiation sources [33–37] and dynamic compression of matter by laser ablation pressure are suitable techniques [38–47]. The resulting HED physics conditions are often characterized by material pressures of 1 mega bar (100 GPa) and above [48]. In the high-density part of the phase space there is also significant overlap with conditions produced at the largest facilities such as the National Ignition Facility (NIF), the Omega laser, or the *Z* pulsed power facility (e.g. [49]).

Fusion research aims towards producing confined burning plasmas with temperatures and densities where heavy isotopes of hydrogen fuse to helium nuclei and neutrons producing 17.6 MeV energy per fusion reaction. This process powers the Sun and has led to all life on earth. The present worldwide effort generally pursues two complementary efforts where hot dense plasmas are confined by magnetic fields or by inertia and heated to fusion temperatures that are typically in the range of 5–50 keV (1 eV = 11 605 K) [50]. The understanding of the physical properties of fusion plasmas and the material and target conditions involved in producing and confining the plasma is of critical importance for the successful demonstration of a laboratory fusion concept and potential future developments as energy source. Key to these research efforts is the application of computer simulations that rely on equation of state (EoS) data and physics models describing thermal transport, thermodynamic equilibrium and hydrodynamic instabilities [51]. The physics becomes important at various stages of the formation of the plasma that follows trajectories through the phase space accessible at the MEC instrument [40].

In addition, to direct LCLS x-ray heating or laser dynamic compression techniques, a 30 TW Ti:sapphire short pulse laser beam has recently become available at MEC. This laser will be further upgraded to a 200 TW class system. This

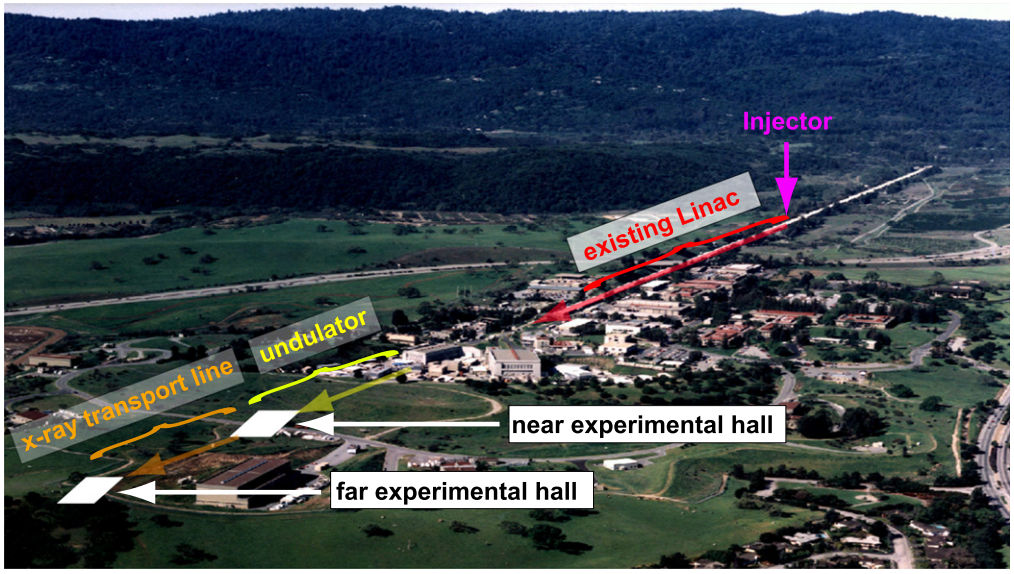

Figure 1. Areal view of the linac coherent light source. Electrons are injected at the 2 km point of the Linac that accelerates electron bunches over 1 km to energies ranging from 4.3 to 14 GeV. A 130 m long undulator is then producing the free electron laser x-ray beam through self amplified spontaneous emission of radiation (SASE) or through self-seeding. Energies are ranging from 1.1 Å to 15 Å at 120 Hz for experiments in the near and far experimental halls. The MEC is the 3rd instrument in the far experimental hall that is reached after a 200 m long x-ray transport line. At MEC, the x-ray beam can deliver x-ray energies from 480 to 11 000 eV with pulse durations of approximately 20 to 500 fs and up to 2 mJ energy per pulse.

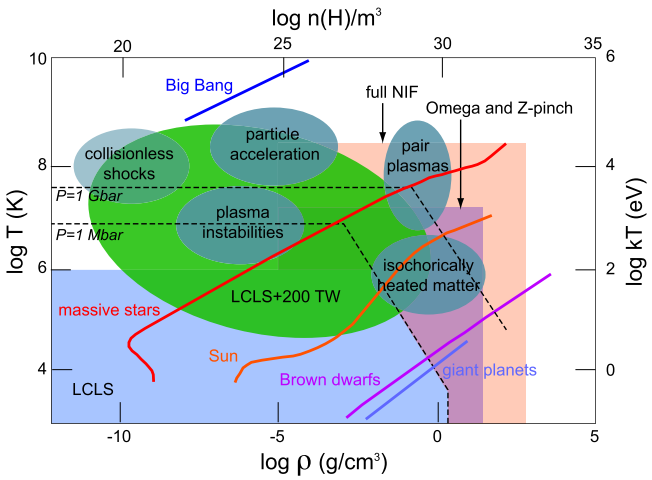

Figure 2. The range in temperature–density phase space is shown that can be produced with LCLS (beige), with LCLS and long pulse lasers, and with a 200 TW high intensity ultra-short pulse laser coupled to LCLS (green). The combination with the LCLS x-ray beam provides world unique experimental capability that will allow studies of laser–plasma interactions, coupling and heating of fusion plasmas, and the demonstration of the physics mechanism for the generation of intense radiation and particle sources by high power lasers. Also shown is the phase space covered by the Omega laser, the *Z* pulsed power facility, and the National Ignition Facility (NIF) laser facility (adopted from [49]).

capability is of particular interest for studies of conditions including those relevant to energetic phenomena in astrophysics [12, 18], for producing sources of intense radiation and for studies of their interaction with matter. Specifically, high-power short pulse lasers produce high-temperature plasmas and relativistic electrons that propagate along filaments and lead to energetic particle beams [9]. Extremely high magnetic fields surround the filaments and affect energy transport and ionization. The target interior is also an intense source of positrons and high-energy photons, x- and γ-rays. LCLS will allow us to probe these conditions and to optimize their use as sources for interaction physics studies.

Central to studies of the high-power laser beam interactions with matter is the on going development of accurate and precise experimental pump–probe and diagnostic techniques. This is required to provide critical experimental tests of simulations and theory of matter in the HED state and further to uncover the underlying physics mechanisms that determine the coupling of ultra intense photon and particle beams with matter.

Figure 3 shows schematics of MEC studies with LCLS. High-energy x-ray pulses are required to penetrate through dense plasmas and to provide *in situ* measurements of the target conditions. The x-ray beam must provide sufficiently large numbers of photons in femtosecond pulses to allow scattering experiments in single shots during the short-lived states of the dynamically evolving plasma. Further, focusing of the beam to small volumes will allow unprecedented spatial resolution in studies of matter at HED and will resolve previously unexplored energy and particle transport properties. Novel combinations of high-power laser beams, laser-produced radiation, and multiple x-ray pulses with multiple x-ray energies at sub-nanosecond delay will open up novel pump–probe capabilities for resolving the evolution of extreme matter states towards or away from equilibrium.

The method of production of extreme matter states can vary from the direct irradiation of a sample by the LCLS or a

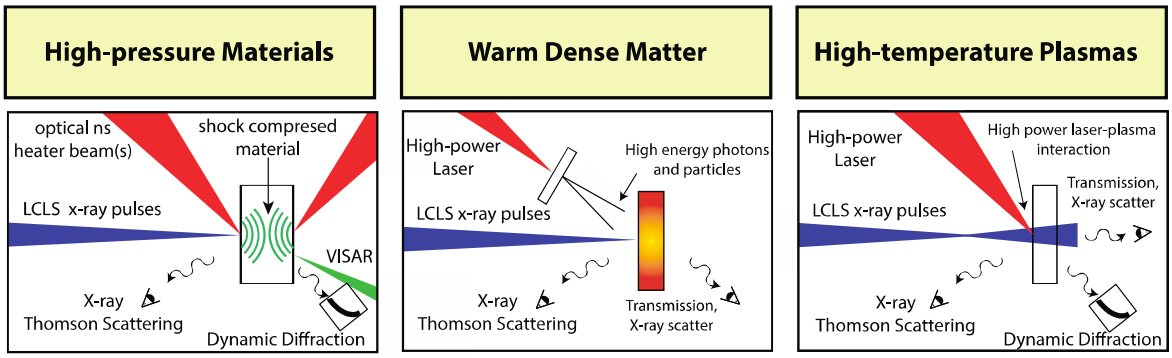

Figure 3. Examples of geometries are shown for investigations of matter in extreme conditions with ultrafast pump–probe experiments at LCLS.

high-power short pulse laser of thin (1 nm–10 000 nm) samples, the irradiation of thicker samples by long pulse lasers to compress samples, or the interaction of energetic particle beams produced by short pulse laser focused to high intensity ($>10^{16}$ W cm^{-2}).

The first experiments on the MEC instrument have investigated laser-compressed solids. They address a wide variety of topics in high-pressure research including shock waves, equation-of-state, shock-induced chemical reactions, strength kinetics, dislocation dynamics, high strain rate phenomena, or plasmon and phonon dispersion [52–54]. Dynamic high-pressure experiments utilize nanosecond long pulse laser beams focused onto a target, to spot sizes of 50–400 μm using phase plate beam smoothing conditioning. The beams compress solid targets by ablation pressures in the mega bar pressure range, see figure 3 (left). X-ray scattering and dynamic diffraction measurements determine the properties of the HED state and can be complemented by shock and particle velocity characterization in the laser-driven target using a velocity interferometer system for any reflector (VISAR) [55], and a Fourier domain interferometer (FDI) [56]. These optical measurements characterize reflective surface motions from shock or compression waves and target surface expansion.

The recent addition of the high-power short pulse laser to MEC greatly enhances the capabilities for ultrafast pump–probe studies allowing direct x-ray probing of high-power laser interaction with matter or optical probing of x-ray heated systems, see figure 3 (right). In addition, secondary photon and particle beams are now becoming available for interaction studies with warm dense matter (WDM) or to study the dynamic heating into the WDM state using the LCLS x-ray beam, see figure 3 (middle). WDM is a state of matter that is close to solid density, but with temperatures ranging from a couple of eV to tens of eV. In this state, standard plasma theories are not valid as the matter is too dense and cold, and neither are solid-state theories because the thermal energy is of the same order as the interaction energies between atoms and perturbation theory breaks down. Despite its transient small-scale character in laboratory experiments in, e.g., laser- or beam-produced plasma experiments, WDM is found abundantly in nature, for example in steady state conditions in interiors of large planets and accretion disks, or in transient conditions during large (meteor) impact events.

This paper reviews the first LCLS experiments that have investigated high-pressure states in single shot mode. Of particular importance for successful studies of HED matter are independent measurements of temperatures, densities and ionization state. For this purpose, MEC provides the capability for spectrally resolved x-ray Thomson scattering (XRTS) measurements. This technique was first developed using backscatter geometries accessing the non-collective Compton scattering regime that provides information on the microscopic physics by measuring the free electron distribution function [20, 35]. At low-temperatures and small degrees of ionization, the free–free Compton feature blends with bound-free scattering and the data interpretation becomes complex requiring additional information of finite-temperature bound wave functions and continuum lowering. On the other hand, the unique high-peak brightness properties of the LCLS x-ray laser are well suited for collective forward scattering on plasmons whose spectra yield temperatures and densities with unprecedented precision at micron-scale resolution in dynamic compression experiments. The plasmon scattering spectrum is of fundamental interest because it holds promise to determine plasma parameters and the physical properties from first principles using the plasmon dispersion and the principle of detailed balance. These techniques have been developed at LCLS utilizing high repetition rates of 120 Hz measuring quasi noise-free plasmon spectra within 7 s [21, 57]. Subsequent single shot measurements in dynamic compression experiments [22] have measured temperatures and densities providing data needed to infer pressures and compression.

Our experiments are precise enough to critically test theory of dense plasmas achieving an accuracy of the elastic scattering feature data that can clearly distinguish between the results of simulations and various theoretical models [58–63]. The LCLS beam visualizes the evolution of the compressed material lattice across the melting line and the coexistence regime into a WDM state [22]. The x-ray diffraction measurements provide structural measurements in these different regimes. In particular for the WDM states, the data reveal a narrow scattering peak that can be interpreted as the combined effects of screening and short-range repulsion (SRR) in the

ion–ion interaction potential [58]. The measurements test predictions from density functional theory coupled to many particle molecular-dynamics (DFT-MD) simulations [60–64]. Up to now, these simulations were used to predict physical properties derived from optical observations of particle and shock velocities. Here, structural and physical properties that are sensitive to many-particle electron–ion (e–i) and ion–ion interaction physics have been obtained. An independent theoretical analysis using pseudo-atom molecular dynamics [65, 66] has shown excellent agreement with the LCLS data when using Kohn–Sham DFT. However, the Thomas–Fermi (orbital free) form of DFT was found to show significant discrepancies, while the hyper-netted chain (HNC) approximation for the Ornstein–Zernike equations was found to be marginal [67].

The experimental data further allow a direct calculation of macroscopic material properties. Especially equation-of-state data can be derived on the shock Hugoniot together with new off-Hugoniot data that occur by shock coalescence. We find that they approach an isentrope and are in agreement with the DFT-MD simulations performed for the measured temperature and density values of the experiment

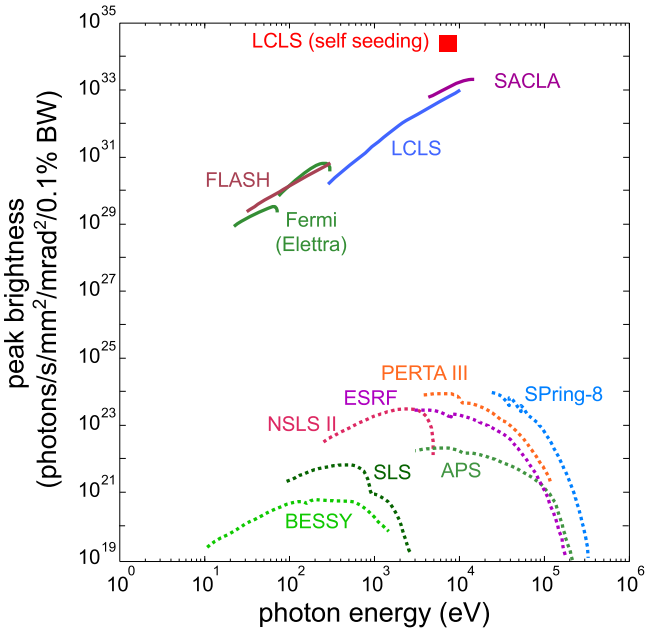

Figure 4. Comparison of peak brightness of various x-ray light sources is shown. An internally self-seeded beam at record peak brightness provides the required photon flux to measure scattering spectra and diffraction data in single dynamic compression experiments and provides the spectral bandwidth to resolve plasmons spectral features.

2. Overview of the MEC instrument at LCLS

2.1. LCLS x-ray beam

LCLS utilizes one third of the 3 km long SLAC Linac [68] to accelerate electrons with a single bunch charge of 150 pC up to approximately 13.6 GeV electron beam energy. During a single pass through a long (100 m) undulator, this pulse will initiate fee electron laser (FEL) action at the undulator fundamental wavelength, which will be tunable between 15 Å and 1.5 Å. The FEL will either operate in self-amplified spontaneous emission (SASE) mode or in a seeded mode. In SASE mode, the FEL radiation field will arise from amplification of the spontaneous undulator radiation created at the start of the long undulator resulting in a bandwith of approximately 40 eV at 8 keV. The seeded LCLS x-ray beam will result in a bandwidth of about 1 eV at 8 keV. Thus, the spectral resolution in seeded-beam LCLS scattering experiments will be limited by the x-ray spectrometer.

To resolve the electron plasma (Langmuir) oscillations [69], we operate LCLS in the seeded x-ray mode a just recently invented tool [26]. In this study, we developed 8 keV peak brightness radiation of 2.7×10^{34} photons $s^{-1}\,mm^{-2}\,mrad^{-2}$ 0.1% bandwidth at LCLS, see figure (4). Within the first 15 undulators the Linac produces SASE with 1 GW power. The electron beam is then passed through a 4 m long chicane while the x-ray beam traverses a diamond crystal that Bragg reflects a narrow energy range of x-rays with a bandwidth of $\Delta E/E = 0.5 \times 10^{-4}$ in the center of the broad SASE spectrum. The diamond (400) reflection was chosen as the wake monochromator for suitable crystal perfection, angular width and low absorption. Thus, the transmitted x-ray spectrum creates a 5 MW trailing monochromatic seed pulse, which has been amplified to ultrahigh peak brightness and total power of 10–15 GW in the subsequent 17 undulators. The resulting record peak brightness x-ray beam is then transported and focused into the dense laser-driven target.

The operational phase has shown that the normal operation of hard x-ray self-seeding performs better with the nominal 150 pC charge and the corresponding 50 fs pulse duration. The stability is improved by roughly a factor of two compared to low charge 20 pC operation with a similar reduction in the per pulse energy fluctuations. In this mode, the pulse energy of the seeded beam is significantly improved with the longer pulse (higher charge) mode. Recently, multi-pulse, multi-color x-ray pulses have been delivered in this mode [70]. The seeded beam normally gives a 2–4 times improvement in time-averaged x-ray power compared with a post-monochromator of similar bandwidth with similar pulse durations and shot-to-shot intensity fluctuations. The narrow seeded line, 0.4–1.1 eV full-width at half maximum, for a 50 fs pulse duration typically contains an average pulse energy of 0.3 mJ, with occasional shots up to 1 mJ. The peak brightness of 2.7×10^{34} photons $s^{-1}\,mm^{-2}\,mrad^{-2}$ 0.1% BW is calculated from the measured pulse duration and a mean pulse energy of 0.3 mJ.

2.2. MEC x-ray instrumentation

The particular strength of the MEC instrument [23] is to combine the LCLS x-ray laser beam with high power optical laser beams [71], and a suite of dedicated diagnostics tailored for HED science. They include two x-ray scattering spectrometers for forward collective and backward non-collective scattering, emission spectrometers and interferometer

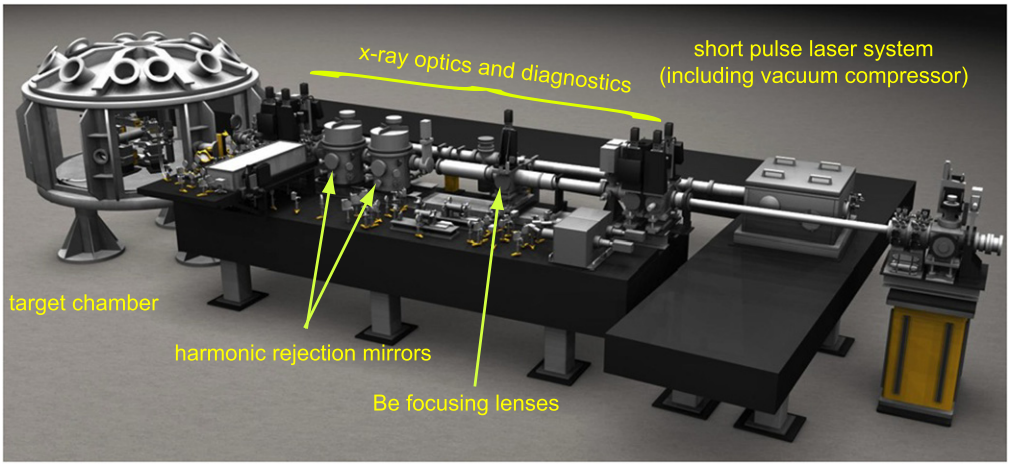

Figure 5. (Left) The x-ray beam is transported 200 m between the near and far experimental halls and combined with high-power lasers at the MEC instrument at the end of the facility. (Right) The x-ray beam is focussed by compound beryllium lenses into the center of the target chamber. The beamline further consists of third harmonic rejection mirrors, x-ray beam intensity, profile, and positioning monitors. Also shown is the path of the short pulse laser system. The long pulse lasers enter the target chamber at an angle of 90° to the x-ray beam axis and can be redirected inside the target chamber using 2″ optics (not shown).

systems. While the vacuum target chamber makes the end-station very versatile, it has been designed to service key scientific areas including WDM physics, high-pressure studies, and laser–plasma interactions.

MEC is the third instrument in the FEH delivering a focused x-ray beam in the energy range $4 < E_{\text{x-ray}}$ 1st < 11 keV for 1st harmonic experiments or $10 < E_{\text{x-ray}}$ 3rd < 25 for experiments with 3rd harmonic beams. A selection of compound refractive lenses can be inserted in the beam to provide focusing at target chamber center for the selected x-ray energy. By locating the sample at or out of focus, the beam size at the sample can be selected from about $\sim 3\ \mu$m to several tens of microns. Figure 5 indicates the location of the instrument in the FEH and a schematic of the x-ray focusing and short pulse laser systems.

Figure 6 shows a schematic of the x-ray beam characterization tools in MEC and examples of x-ray near and far field images from CCD and imprint data. The x-ray focusing capability is a prerequisite for high spatial resolution x-ray imaging and for controlled x-ray scattering measurements in a well-defined target volume. Further, the high photon flux allows direct isochoric x-ray heating of matter that can be probed by, e.g., two-color x-ray probing or ultrafast optical laser measurements. The latter requires accurate cross timing of x-ray and optical laser beams, which can be achieved with an uncertainty of approximately 50 fs.

2.3. Target configurations

The existing target chamber at MEC allows for great flexibility of the x-ray focus location, the optical laser mirror and lens locations, diagnostic instruments, and targets options. Ongoing experiments at the Titan [39] and Trident [72] laser facilities have previously demonstrated a subset of experimental configurations and target types in the same target

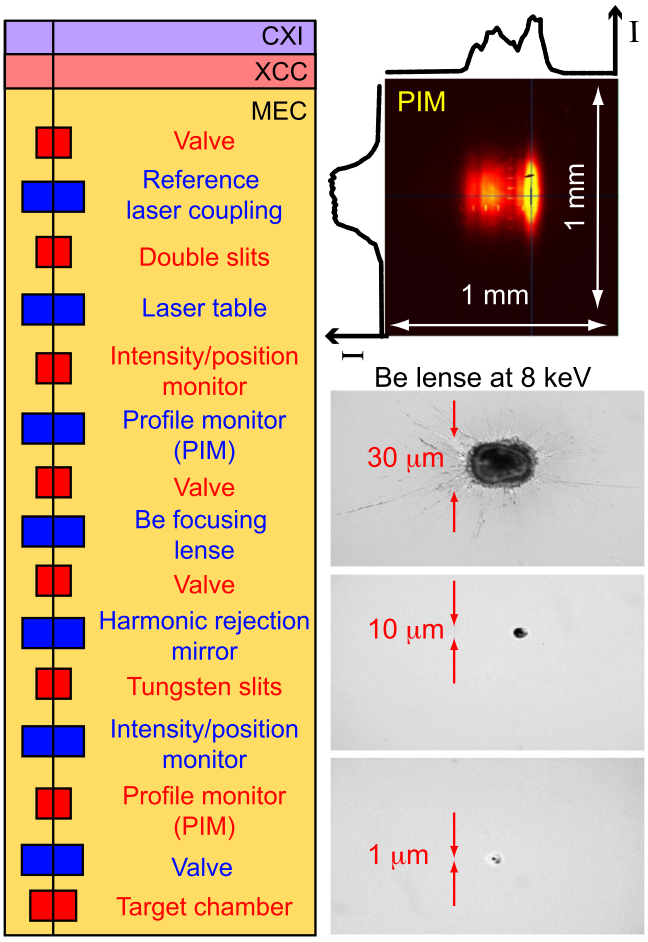

Figure 6. (Left) A schematic is shown of the x-ray beam transport optics and x-ray characterization tools at MEC. (Right) Example of x-ray near field intensity distribution is shown before entering the target chamber. Also shown are examples of x-ray focal spot measurements using imprints on targets coated with 100 nm thick Au layers.

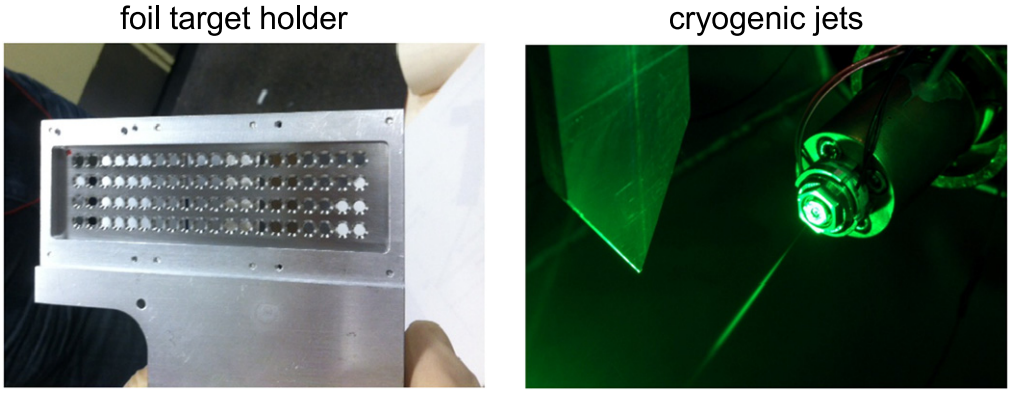

Figure 7. (Left) The target holder is shown for solid target experiments. The long pulse lasers heat the foil that is mounted in one opening in a single dynamic compression experiment. Subsequent experiments use a new foil target in the next opening. (Right) An example of a continuous cryogenic jet is shown. These targets allow experiments at high repetition rates. Pump–probe studies using LCLS combined with the short pulse laser have been demonstrated at 5 Hz.

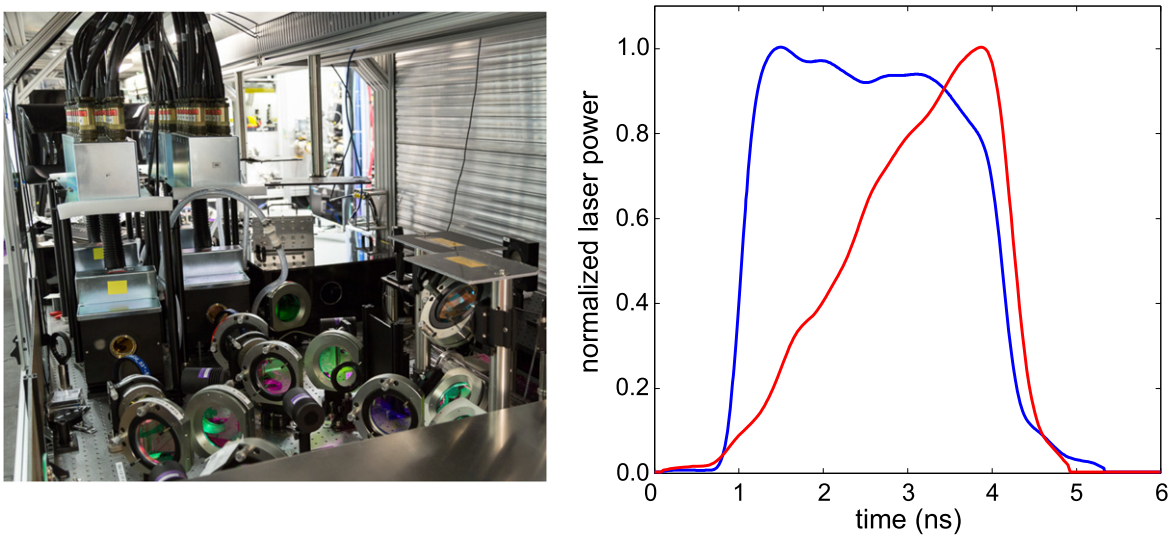

Figure 8. (Left) Picture of MEC Nd:glass laser system showing the 25 mm rod amplifiers. A laser pulse shaping system delivers about 4.5 J in 3 ns per beam on target at 527 nm. (Right) Examples of laser pulse shapes are shown for shock (blue) and ramp wave (red) compression experiments.

chamber architecture. Here, the LCLS x-ray beam will be a new feature increasing the complexity of the experimental platforms and laser set up. Further, the high repetition rates of LCLS of 120 Hz require new developments in target delivery to fully utilize the x-ray capabilities. Figure 7 shows two examples of target capabilities that have been successfully fielded at MEC.

The solid-density target holder provides thin foils for experiments where strong shocks have been launched on either side by ablation pressure produced by the nanosecond laser beams. The shocked matter temperature and density conditions and the shock speeds will be probed with spectrally, temporally and wavenumber resolved x-ray scattering and optical measurements on targets irradiated on either side or by a single beam from one side.

For this class of experiments, the shot repetition rates are limited by (1) target alignment time and (2) by the cooling time of the glass rod amplifiers. Here, it should be noted that when using the x-ray beam alone, 120 Hz experiments have been demonstrated because the foil is heated by the x-ray beam locally over diameters of several 10 μm and can be rapidly translated orthogonal to the x-ray beam axis to deliver a new target surface for subsequent shots, see [21, 57].

More recently, continuous cryogenic liquid jets have been developed and fielded at MEC. First experiments used hydrogen for laser–plasma experiments with densities of 0.07 g cc^{-1} ($n_0 = 4.2 \times 10^{22}$ cm^{-3}), see figure 7 (right). This capability allows experiments at high repetition rates for structural investigations and ultrafast heating studies. Typical jet diameters are between 8 and 20 μm [31, 32], with recent developments towards smaller diameter jets being under way. Other demonstrated cryogenic jet targets include argon, CO_2, and deuterium.

2.4. Optical high-power laser systems

2.4.1. Long pulse Nd:glass laser. MEC is equipped with two frequency doubled Nd:Glass laser systems [23, 71] that each

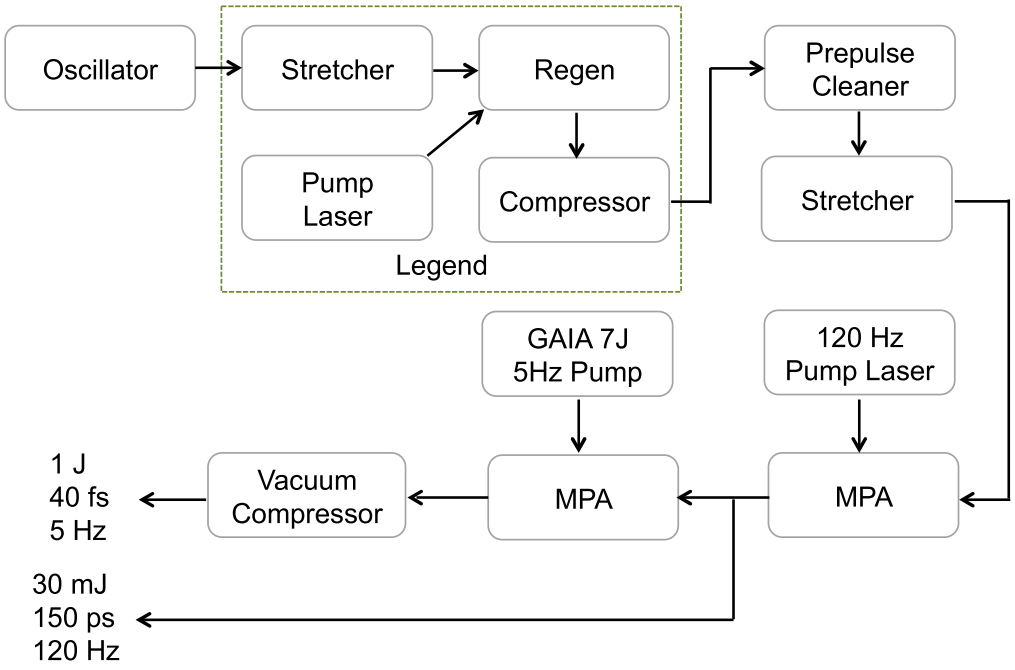

Figure 9. Schematic for two different modes of short pulse laser operations at MEC is shown. Pulses at 30 mJ can be delivered at 120 Hz to match the LCLS x-ray beam repetition rate. A higher 25 TW laser power option exists at 5 Hz.

deliver green (527 nm) light on target with energies up to 18 J for pulse durations larger than 15 ns. For typical applications with pulse lengths of several nanoseconds, the peak laser power is 1–2 GW per beam with variable pulse shaping and rise times of 0.5–1 ns see figure 8. The arrival time of the optical laser beams with respect to the x-ray beam can be changed during the experiment, and is accurate within 25 ps rms. Typical repetition rates for the Nd:glass laser are 1 shot every 7 min when using both lasers simultaneously.

To access a broad range of interesting regimes by dynamic compression it is desirable to further improve the existing systems. At highest priority is increasing the total laser energy on target, to provide precision laser pulse shaping, and shot-by-shot pulse monitoring with the goal to drive larger samples with spatially flat topped intensity profiles for planar shocks. In addition, cross timing and equivalent plane focal spot monitoring will enable measurements of the laser-beam uniformity at the plane of the target. For this purpose, the monopotassium phosphate frequency doubling crystals may be replaced by lithium triborate crystals for a 30% increase of laser energy on target. In addition, for tailoring the focal spot profile on target a suite of phase plates are available to deliver spot diameters in the range of 50 μm $< d <$ 400 μm. To further reduce the effects of laser-beam non-uniformities experiments on solid targets have employed low-Z ablators of varying thickness from 2 μm $< d <$ 50 μm. Future improvements in laser technology and additional amplifier stages for delivering increased laser energy on target will be important to continue accessing important new regimes of the HED phase space, see figure 2.

2.4.2. Short pulse Ti:sapphire laser. The existing MEC short pulse laser system is shown schematically in figure 9. The system is capable of producing 1 J pulses with a temporal width of 40 fs, and thus delivers a peak power of 25 TW. When focused to $a \sim 5$ μm spot size on a target, this provides peak intensities in the relativistic regime where the electron quiver velocity approaches relativistic velocities, i.e. at intensities exceeding 10^{19} W cm^{-2}. The repetition rate of this system is determined by the final amplifier GAIA pump laser and is currently 5 Hz.

At relativistic laser intensities, the contrast ratio between the main pulse and any possible pre-pulses or pedestal pulses is important. To reduce the pre-pulse intensity a cross-polarized wave generator (XPW) has been implemented. In this case, the pulse is compressed after the regenerative amplifier (Legend). The resulting short pulse can then be cleaned in a saturable absorber or XPW device. These pulse 'cleaning' techniques have demonstrated contrast ratios in the 10^{10} range, albeit at the loss of pulse energy. To compensate the loss an additional multi-pass amplifier (MPA) has been added. Because these MPA are pumped by CW diode-pumped Nd:YLF lasers, they provide an exceptionally stable, typically better than 0.2% rms energy stability, and a near perfect Gaussian spatial profile. Because these lasers run at 120 Hz, this will provide the option to have lower energy 30 mJ short pulses at 120 Hz to match the pulse rate of LCLS. The addition of a MPA that can be pumped by a 7 J, GAIA laser provides higher-energy high-power experiments at 25 TW albeit at reduced repetition rates of 5 Hz.

The system can be further upgraded to 200 TW peak laser power by adding a third MPA to the laser to be pumped by the MEC nanosecond laser. At this stage, larger diffraction gratings may be needed in the pulse vacuum compressor in order to accommodate the increased energy without damage. Also, a deformable mirror and wavefront sensor system will be

fielded to optimize the wavefront for the tightest possible focal spot. This should provide 6–8 J of output energy in a ~45 fs pulse width with good spatial wave front and temporal contrast. This high-power laser will produce focused peak intensities in the 10^{20} W cm^{-2} range at a repetition rate that is defined by the nanosecond laser at 1 shot every 3–10 min. It may further be possible to develop a burst mode which will deliver a 0.01 Hz shot rate followed by an extended cool down period that may be used for other experimental activities.

2.5. Diagnostic systems

2.5.1. General description. The size of the MEC target chamber with a radius of 1 m provides sufficient space to place in-vacuum optical and x-ray diagnostics. An extensive suite of x-ray scattering diagnostics is available including highly efficient graphite crystal spectrometers for single shot measurements of scattering spectra, high-resolution spectrometers for x-ray emission and absorption measurements, and areal detectors for angularly resolved scattering measurements, and phase contrast imaging. The suite of x-ray diagnostics is complemented by optical measurement capabilities, FDI and VISAR. In addition, high magnification optical backlighting has been applied using the optical short pulse laser. For alignment purposes, questar long distance microscopes are available providing a field of view of 0.5–5 mm with a spatial resolution of 7 μm. Below, we discuss examples of x-ray and optical measurements applied during the first shock-compressed matter experiments at MEC.

2.5.2. Spectrally-resolved x-ray scattering

2.5.2.1. Highly annealed pyrolytic graphite (HAPG) spectrometer. To maximize the collection fraction, x-ray scattering experiments require spectrometers with high efficiency, but with high resolving power of $\Delta E/E < 10^{-3}$. In the multi-keV x-ray regime, artificial crystals from low-Z materials such as carbon with a mosaic spread of ~0.1° approach these requirements. To further improve collection efficiency the distances from the crystal to both source and detector are typically chosen to be the same, resulting in mosaic focusing and high spectral resolution [73]. In addition, a cylindrically bent crystal in von-Hamos geometry will further optimize collection by about a factor of 2 [74].

At MEC, HAPG crystals have been fielded [75, 76]. These crystals have been shown to provide advantages over previously used HOPG [74, 77]. The point-spread function is dominated by so-called depth broadening. Due to negligible photo-absorption (the attenuation length of 8 keV x-rays in C is about 1 mm), x-rays penetrate deep into the crystal until they encounter a crystallite that is properly oriented to reflect the ray. In von-Hamos geometry, a x-ray point source will therefore be broadened in the detector plane and in the dispersion plane by $2D/\tan(\theta_B)$ with the crystal thickness D and the Bragg angle θ_B. Ray tracing simulations for a point source and monochromatic 8 keV x-rays have been performed for HAPG crystals of 30 × 30 mm^2 size and 51.7 mm radius of curvature ($\theta_B = 13°$). The calculations show that the point spread function of the 40 μm thick crystal is about 6 eV wide with $E/\Delta E = 1300$ suitable for resolving plasmon scattering spectra in dense plasmas. This crystal has been used for the forward scattering measurements. In backscatter, a 100 μm thick crystal has been employed with lower spectral resolution of 14 eV and $E/\Delta E = 550$. This crystal results in a higher reflectivity, as determined by the integral over the reflection curve. Some decrease of reflectivity in the high-photon energy tail is observed due to photo-absorption in the crystal volume.

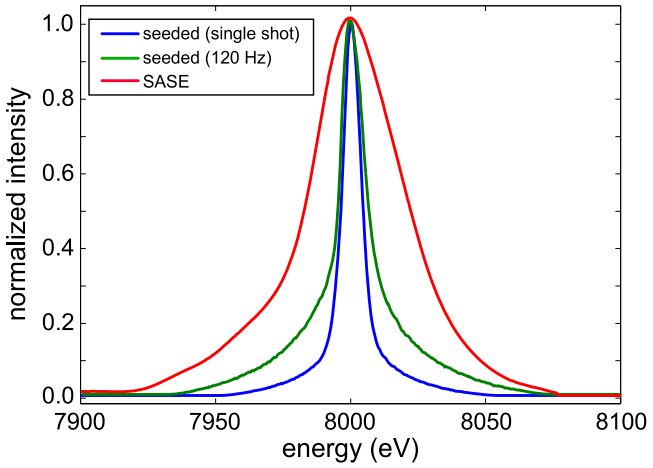

Figure 10. The HAPG instrument function is shown for a 40 μm thick crystal used for forward (plasmon) scattering experiments. The single shot profile is compared with the one obtained when averaging of 700 seeded beam shots with slightly fluctuating energy at a high-repetition rate. These spectra demonstrate a spectral resolution of 0.1%.

Figure 10 compares the instrument function for a single shot with the one for experiments that average over 700 shots with a seeded x-ray beam. Here, we observe that statistical fluctuation in the x-ray laser energy result in additional broadening of the effective profile. Even when taking these fluctuations into account the diagnostic is well suited for resolving the plasmon scattering spectrum and the plasmon frequency shift.

2.5.2.2. Plasmon measurements. Plasmon measurements were first validated at MEC utilizing high-resolution measurements from isochorically heated targets at 120 Hz repetition rates. Subsequently, the technique was applied for single shot measurements on shock-compressed aluminum. Figure 11 shows the experimental scattering spectra from solid-density aluminum from Fletcher *et al* [57]. Results are shown from the forward scattering and backward scattering spectrometers with the x-ray beam in seeded and SASE mode of operation. The seeded x-ray beam provides a bandwidth of 1 eV and combined with 8 eV spectrometer resolution resolves the plasmon that is down-shifted from the elastic 8 keV scattering feature by 19 eV.

Further, figure 11 shows the results of the backward scattering spectrometer which observes elastic scattering at 8 keV reflecting the instrument function of the spectrometer convolved with a Gaussian profile that accounts for the

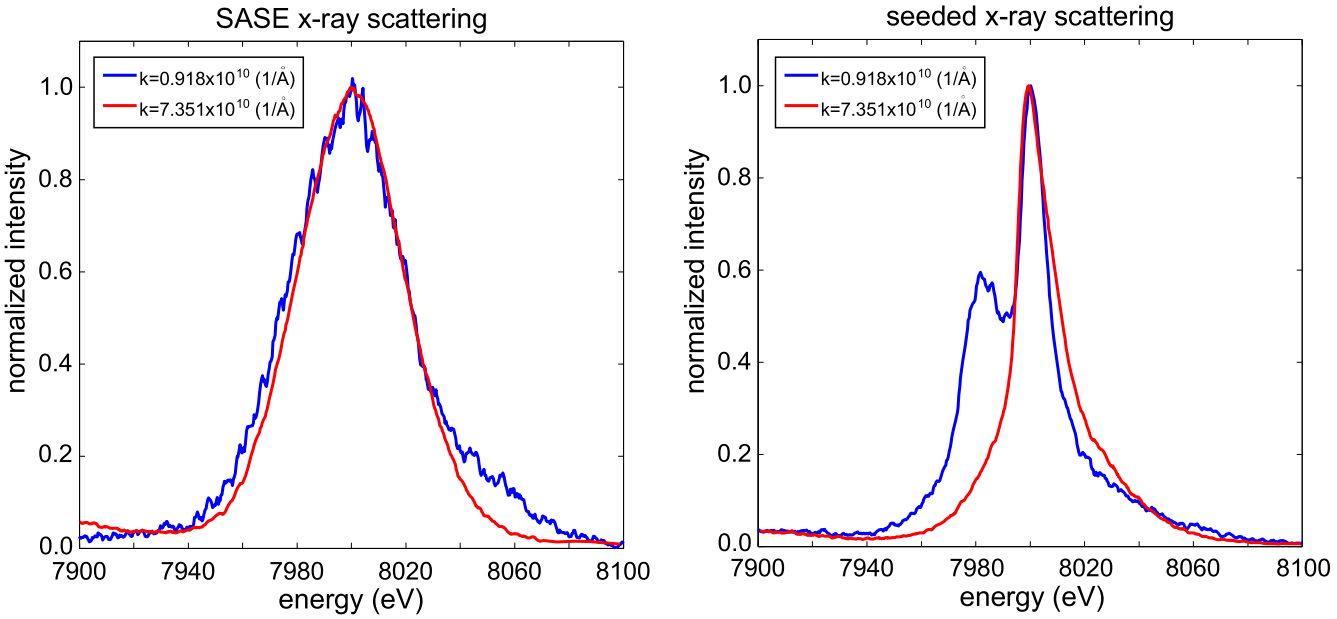

Figure 11. X-ray Thomson scattering data from solid density aluminum targets are shown from forward (plasmon) scattering and backscattering spectrometers for seeded (right) and SASE (left) x-ray beam operation [55]. These data are accumulated over 700 shots at 120 Hz. The data indicate 8 eV resolution for a seeded beam and 50 eV for SASE operations.

statistical fluctuations of the x-ray energy of a seeded beam over 700 shots. These measurements do not indicate an inelastic scattering feature in the vicinity of the plasmon peak validating that bound-free scattering is not affecting the results of the forward scattering measurements; bound-free scattering features are predicted to be negligible in this energy range and no feature has been observed with the back-scattering spectrometer. For these measurements, the crystal in the forward scattering spectrometer is 40 μm thick while in backscattering we employed a 100 μm thick crystal giving rise to slightly different instrument functions and consequently slight differences in the spectral shape of the elastic scattering feature.

Because the x-ray seed power is generated from the random SASE process that fluctuates in energy and amplitude, less than $1/3$ of the shots provide sufficient photons with adequate spectrum for single shot x-ray scattering experiments. When summing over 700 shots the spectrum shows a broad foot, but the bandwidth is mostly preserved greatly improving the resolution when compared to the SASE spectrum. In forward direction, the x-ray scattering spectra with SASE operation show a slight broadening of the red wing of the scattering spectrum, see figure 11, but the SASE scattering spectrum is not suitable for inferring the dense plasma conditions.

Figure 12 shows the theoretical fit of the dynamic structure factor, see section 3, to the experimental forward scattering spectrum. The shift of the plasmon peak yields the electron density of $n_e = 1.8 \times 10^{23}\,\mathrm{cm}^{-3} \pm 5\%$. The electron temperature of the fit is 2 eV accounting for the isochoric heating of the aluminum by the x-ray laser pulse [22]. The ions are cold with temperatures of order 0.1 eV consistent with the observation of Debye–Scherrer rings from solid

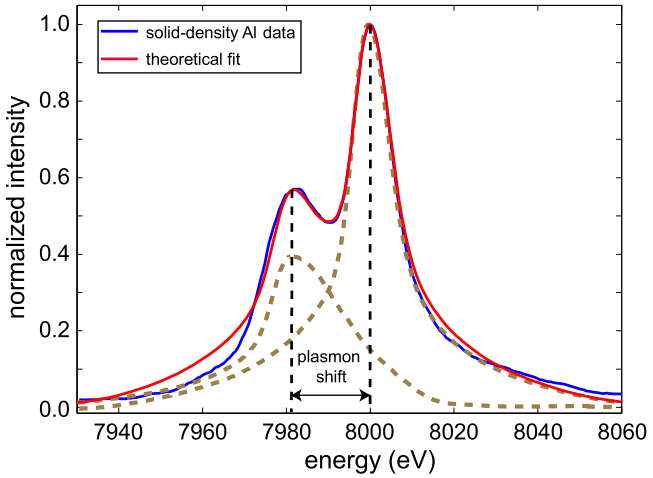

Figure 12. The theoretical fit to the experimental forward x-ray plasmon scattering data from solid-density alimunum is shown for the electron density of $n_e = 1.8 \times 10^{23}\,\mathrm{cm}^{-3}$. In these near Fermi-degenerate states, the theoretical fit of the plasmon feature is not sensitive to the electron temperature; however, the intensity of the elastic scattering feature at 8 keV depends on both electron and ion temperature. The dashed curve centered at 8000 eV shows the elastic scattering component and the dashed curve centered at 7981 eV represents the plasmon spectrum.

aluminum. Here, the plasmon frequency is extremely sensitive to the electron density, but temperature effects are too small to affect the plasmon energy shift. The accuracy of the electron density measurement is very high due to the sensitivity of the plasmon resonance to the plasma frequency. With $n_e = Z/A\ 6.03 \times 10^{23}\ \rho$ (the electron density n_e in cm^{-3} and the mass density ρ in $\mathrm{g\,cm}^{-3}$), assuming the ionization state of $Z = 3$ and using the mass $A = 26.98\ u$, the

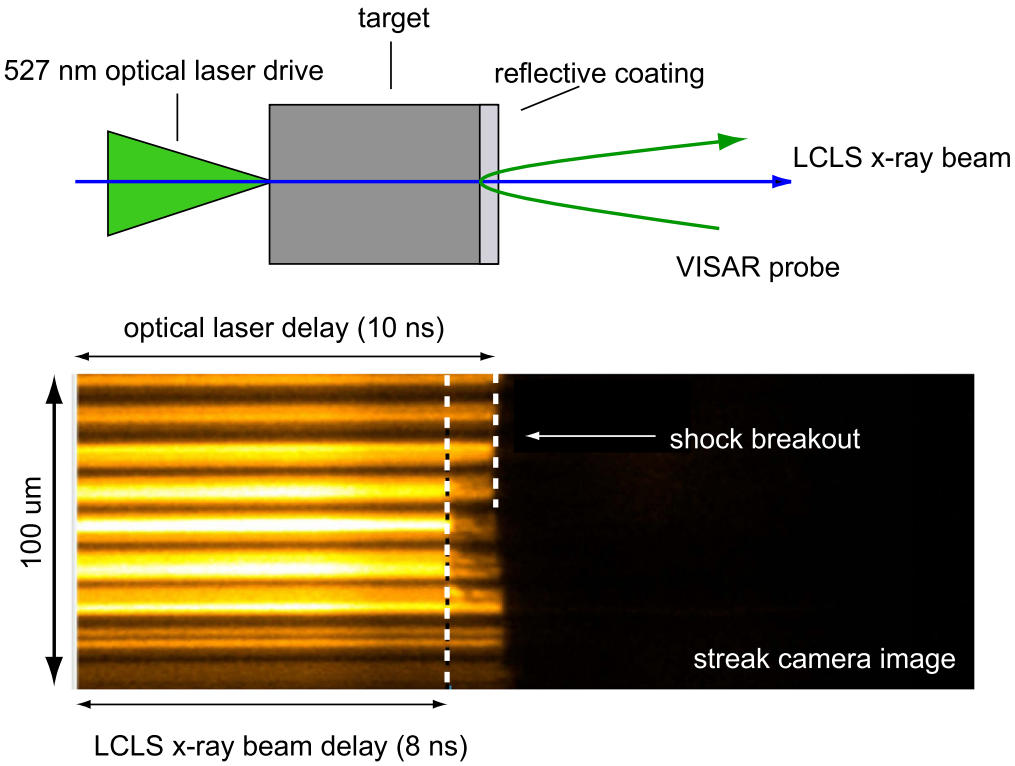

Figure 13. An example of a VISAR streak camera record shows the drop in the fringe intensity due to the heating of the rear surface by the LCLS x-ray beam. These measurements provide timing and location of the x-ray beam with respect to shock break out.

measured electron density results in $\rho = 2.7\,\mathrm{g\,cm^{-3}}$ as expected for solid aluminum.

2.5.3. VISAR system. The MEC instrument is equipped with a line imaging VISAR system for velocity measurements of rapid surface motions that are typically in the range of 1–20 km $\mathrm{s^{-1}}$. This diagnostic tool obtains accurate continuous velocity-time histories of surface motions. The VISAR measures velocities by using the Doppler shift of a green laser beam diffusely reflected from the moving surface. The reflected light is collected and collimated into a Michelson-type interferometer. The imaging field of view is 0.5–1 mm with a spatial resolution of 10 μm. The interferometer splits the light into equal parts so that the apparent optical path lengths of the two arms are equal to allow interference of spatially incoherent light, but at the same time with light from one arm delayed in time so that fringe shifts occur with wavelength changes. These requirements are satisfied by the use of an etalon in one arm. At MEC, several etalons of 25 mm diameter and with varying thickness between 5.072 mm–15.01 mm and of 50 mm diameter and with varying thickness in the range of 25.036 mm–75.04 mm are available. Two Hamamatsu streak cameras measure the fringes in two arms with different etalons providing a temporal window of 1 ns–1 ms and temporal resolution of approximately 20 ps. The system can operate at a repetition rate of about 0.1 Hz.

Figure 13 shows an example of a VISAR streak camera record when used in combination with the LCLS x-ray beam. This experiment uses a graphite target irradiated by a 1 TW frequency-doubled drive beam launching a shock wave that propagates through the target. The probe beam reflection from VISAR shows steady interference fringes from the backside of target that is coated with a reflective aluminum surface. The fringes disappear at the time of shock breakout when the optical reflectivity of the surface drops significantly. With exact cross timing of the VISAR probe laser, streak camera and drive laser these data yield the averaged shock velocity. In addition, step targets or wedge targets will provide more accurate measurements of the shock velocity. However, a unique feature can be observed at the time when the LCLS x-ray beam is fired (in this case about ¾ through the optical laser drive). At that time, the reflectivity of the back coating is reduced providing an accurate measurement of both the x-ray probe time with respect to shock breakout and the exact location of the LCLS beam in the target.

3. Theory and simulations

3.1. Dynamic compression using counter-propagating shock waves

3.1.1. Simulations of shock states. Figure 14 shows examples of radiation-hydrodynamic design calculations of shock-compressed solid aluminum experiments that utilize experimental laser powers, pulse shapes and phase-plate focal spots [78] available at MEC. A 2 μm thick CH coating was applied on the laser drive sides. The simulations use the radiation-hydrodynamic code HELIOS [79]. The nanosecond

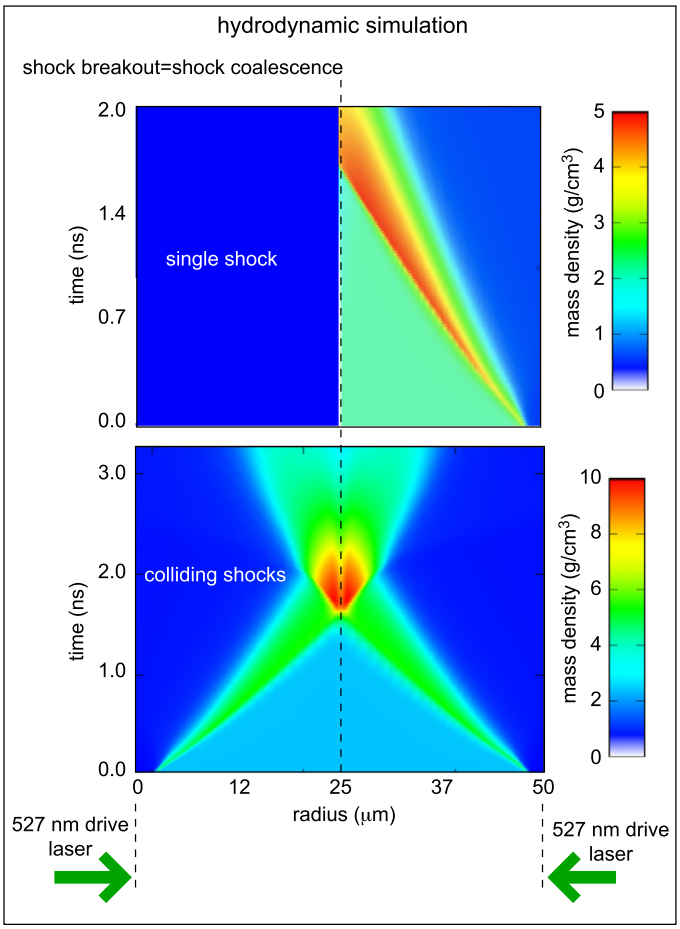

laser parameters

pulse duration	phase plates	laser energy	intensity per arm
3 ns	50 μm	6 J	100 TW/cm^2

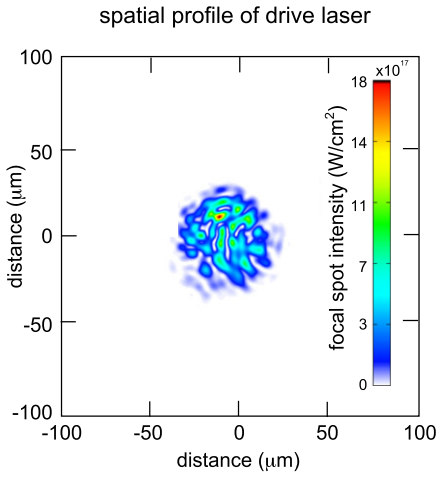

Figure 14. (Left) Radiation-hydrodynamic design of single shock wave experiments and counter-propagating shocks driven by two MEC nanosecond lasers with the same pulse shape. (Right) Laser intensities and focal spot data are obtained from phase plate characterization.

laser beams are frequency converted to green delivering 527 nm laser light on target with the pulse shape shown in blue in figure 8 in a focal spot of approximately 50 μm.

The simulations indicate that the shocks propagate through the solid with an averaged shock velocity of 14 km s^{-1}, traversing 25 μm thick aluminum plus 2 μm CH and break out or coalesce in the center at about 1.9 ns after the start of the laser irradiation. These shock waves initially compress the solid by a factor of 2–3 and during coalescence they reach 4 times solid density and multi mega bar pressures. These conditions can be compared with the Rankine–Hugoniot relations with $\rho_1/\rho_0 = D/(D-u)$, where D is the shock velocity, u is the particle velocity. For two-fold compression, i.e. $\rho_1/\rho_0 = 2$, we infer ½ $D = u$, and with a shock velocity of 14 km s^{-1} (20 km s^{-1}) we obtain pressures of $\Delta P = \rho_0\, Du \sim 2.6$ Mbar (5.4 Mbar). Here, the density and pressure define the Hugoniot curve of the shocked material. Experiments that will simultaneously measure the temperature will determine the thermodynamic state of the shock wave and will be important to estimate heat capacity and energy partition of the shocked material.

3.1.2. Counter-propagating shocks. To reach high compression states of solid targets by intense laser radiation in the laboratory, the technique of coalescing shocks is often applied [39, 44]. It is well known that a large number of shocks with a fixed pressure change results in adiabatic compression also described with negligible entropy changes. At MEC, the counterpropagating shock technique has been applied in experiments that reach several times solid density, temperatures of several 10 000 K, and pressures in excess of 1 Mbar. Here, the entropy largely determined by the conditions in the first shock. These extreme states of matter serve as model systems to investigate the thermodynamic state, the material structure, and the physical (microscopic) properties.

For these studies, the adiabatic exponent $\gamma = (\partial \ln p/\partial \ln \rho)_{S=\text{const}}$ is a central quantity. For perfect gases, $\gamma = c_p/c_v$ is the ratio of heat capacities at constant pressure and volume, respectively. Furthermore, γ determines the sound speed, and the EoS [1, 47, 48, 80–82]. For the examples below we choose $\rho_0 = 2.7$ g cc^{-1}. Here and in the following, we denote conditions in the uncompressed material by the index 0, the single shock compressed matter by index 1, and the region of shock overlap by index 2.

We apply the Rankine–Hugoniot equations [47] to determine the polytropic index γ. We describe each shock by the Rankine–Hugoniot equation which relates the particle velocities u_0, u_1, pressures p_0, p_1 and mass densities ρ_0, ρ_1 in the uncompressed and in the compressed region, respectively

and which follow from the conservation of total mass, energy, and momentum. One finds for the energy jump across the shock front

$$\mathcal{E}_0 - \mathcal{E}_1 = u_0^2 - u_1^2 + \frac{p_0}{\rho_0} - \frac{p_1}{\rho_1} = \frac{1}{2}(p_0 + p_1)(\rho_1^{-1} - \rho_0^{-1}). \quad (1)$$

These relations hold for each individual shock as well as for the two shock fronts that evolve after the shock collision between the single and the doubly shocked material and which travel in opposite directions away from each other. The adiabatic exponent γ is introduced to eliminate the internal energy $\varepsilon = p/(\gamma-1)\,\rho$. Accounting for different values of γ before and after compression, one derives for the compression ratio

$$\frac{\rho_1}{\rho_0} = \frac{1 + (p_1/p_0)\dfrac{\gamma_1 + 1}{\gamma_1 - 1}}{p_1/p_0 + \dfrac{\gamma_0 + 1}{\gamma_0 - 1}}. \quad (2)$$

In the strong shock limit $p_1/p_0 \to \infty$, one recovers the familiar result

$$\lim_{p_1/p_0 \to \infty} \frac{\rho_1}{\rho_0} = \frac{\gamma_1 + 1}{\gamma_1 - 1}. \quad (3)$$

Note that the strong shock compression depends only on γ_1, i.e. the conditions in the compressed region. For a perfect monoatomic gas with $\gamma = 5/3$, one obtains $\lim_{p_1/p_0 \to \infty} \rho_1/\rho_0 = 4$. The pressure ratio is derived from equation (3) as

$$\frac{p_j}{p_i} = 1 + \frac{2\gamma_j - 2\gamma_i \dfrac{\rho_j}{\rho_i}\dfrac{\gamma_j - 1}{\gamma_i - 1}}{\dfrac{\rho_j}{\rho_i}(\gamma_j - 1) - \gamma_j - 1}. \quad (4)$$

The jump in particle velocities can be expressed as

$$(u_i - u_j)^2 = \left(1 - \frac{\rho_i}{\rho_j}\right)\frac{p_i}{\rho_i}\left(\frac{p_j}{p_i} - 1\right). \quad (5)$$

In the case of two colliding strong shocks, symmetry of the problem with respect to the contact surface between the two shock waves at the moment of collision competely determines the final compression [47]. In particular, the material at the contact surface is at rest, $u_2 = 0$. Furthermore, the material velocity in the unshocked material u_0 is negligible compared to u_1, the velocity in the first, strongly shocked material region. For a system with constant heat capacity ratio $\gamma_2 = \gamma_1 = \gamma_0$, one recovers the following result for the second compression:

$$\rho_2/\rho_1 = [2 + (\gamma + 1)(\rho_1/\rho_0 - 1)]/[2 + (\gamma - 1)(\rho_1/\rho_0 - 1)]. \quad (6)$$

For the ideal gas with $\gamma = 5/3$ one finds $\rho_2/\rho_1 = 2.5$. For a system where both density jumps are accurately measured one easily inverts the equations to obtain γ_1 and γ_2. For the example above with $\rho_1/\rho_0 = 2$ and $\gamma_2 = \gamma_1 = 2$ (see [44]), we find $\rho_2/\rho_1 = 5/3$ or $\rho_2/\rho_0 = 10/3$. Further, by varying the laser intensity on both sides of the foil and measuring the density jumps with, e.g, XRTS, a range of conditions can be accessed, and γ can be directly determined.

3.2. Spectrally-resolved x-ray scattering

3.2.1. General description. Spectrally resolved x-ray scattering has emerged as a powerful tool to measure the plasma conditions of dense compressed states of matter and as a core capability to determine the physical properties of MEC. XRTS provides the dynamic structure factor $S(\mathbf{k}, \omega)$, which is central for calculating e–i collisions for wave damping, electrical conductivity, thermal conductivity, free–free opacity, line-broadening, and plasma oscillations. Experiments on laser-produced dense plasmas utilize fast detection of the angular and frequency resolved x-ray scattering spectra. Previous studies at large kilojoule type laser facilities [20, 35–46] have demonstrated spectrally resolved scattering techniques measuring the x-ray Compton backscattering and the plasmon forward scattering spectra providing the temperature and density of the plasma. The temporal resolution achieved in previous studies is about 100 ps using fast framing camera detectors, or about 10 ps using a laser-produced K-α source.

The collimated high-energy LCLS x-ray beam enables novel investigations of HED states using the high photon flux in 50 fs pulses with photon energies of 4–8 keV that are unique to the MEC end station. Experiments with ultrafast 50 fs x-ray scattering techniques and high spectral resolution can now be performed at orders of magnitude higher repetition rates than previous studies so that high signal-to-noise ratios and precision spectral measurements will be achieved. Furthermore, using the LCLS x-ray beam as opposed to laser-produced plasma sources will provide a well-defined incident scattering vector; these facts combined with a seeded x-ray beam with 1 eV spectral bandwidth will provide precision spectra and highly accurate measurements of the scattering features. Combining this unique x-ray capability with powerful lasers allows investigating the microscopic and hydrodynamic physics properties of HED plasmas.

The x-ray scattering process is significantly different from optical scattering [20, 82] because the energy of the incident x-ray photon with frequency ω_0 is large enough to give a significant Compton shift to the frequency of the scattered radiation. During the scattering process, the incident photons transfer momentum $\hbar\mathbf{k}$ and energy $\hbar\omega = (\hbar\mathbf{k})^2/2m_e$

to the electrons. The magnitude of the **k**-vector is given by

$$k = |\boldsymbol{k}| = \frac{4\pi E_0}{hc} \sin\left(\frac{\theta}{2}\right) \tag{7}$$

with $E_0 = \hbar\omega_0$ being the energy of the probe x-rays and θ the scattering angle. Momentum and energy are primarily transferred to the free and weakly bound electrons whose binding energy is less than the Compton energy $\hbar\omega$. In the non-collective (Compton scattering) regime, the contribution of the free electrons that carry the information on the Fermi energy (i.e., electron density) or the electron temperature of the dense plasma is measured in the inelastic scattering feature. Moreover, bound electrons with ionization energies larger than $\hbar\omega$ (states deep in the Fermi sphere) cannot be excited, and no Compton energy transfer occurs during the scattering process.

Thus, the total XRTS spectrum results in elastic and inelastic spectral features that are described by the dynamic form factor, $S(\mathbf{k}, \omega)$ [83]. The ion structure is measured from the un-shifted elastic scattering component at E_0 that is commonly referred to as Rayleigh peak. For the analysis of x-ray scattering experiments, we developed a comprehensive analysis tool [84] that is based on the Chihara formula [85]. The formula describes the contributions to elastic scattering and inelastic scattering from free (delocalized) and weakly bound electrons by the dynamic form factor

$$S(\mathbf{k}, \omega) = |f_I(\mathbf{k}) + q(\mathbf{k})|^2 S_{ii}(\mathbf{k}) + Z_f S_{ee}(k, \omega) + Z_C \int S_{CE}(\mathbf{k}, \omega - \omega') S_S(\mathbf{k}, \omega) d\omega' \tag{8}$$

with Z_f and Z_C denote the number of free and bound electrons, respectively. It is primarily the intensity of the elastic (Rayleigh) peak described by the first term that provides the ionic structure while the intensity and spectral dispersion of the inelastic free-electron scattering described by the second term provides information on the electronic system. The last term of equation (8) includes inelastic scattering by weakly bound electrons, which arises from bound–bound and bound-free transitions to the continuum of core electrons within an ion, $S_{CE}(\mathbf{k}, \omega)$, modulated by the self-motion of the ions, represented by $S_S(\mathbf{k}, \omega)$. The corresponding spectrum of the scattered radiation is that of a Raman-type band. Recently, there has been much activity to improve the theoretical description of this term, e.g., [86, 87]. For plasmon scattering applied in this study, we find that this term is not important when compared to the free electron dynamic structure. Principally, the relative contributions of the bound-free feature (third term in equation (8)) and the free–free feature (second term in equation (8)) can be utilized to infer the number of bound electrons and hence the ionization degree and the density of the dense plasma [87].

We have developed a theoretical fitting code that calculates $S(\mathbf{k}, \omega)$. Where physics uncertainties exist, several theoretical models have been developed for comparisons and to establish sensitivities. They are available for comparisons with experimental data. There are three areas, (1) for term 1, four different models have been implemented for calculations of the ion–ion structure factor $S_{ii}(\mathbf{k})$ to describe the elastic (Rayleigh) scattering peak [88]. They include a Debye model, a one component plasma model and a screened one component plasma (SOCP) approximation with and without negative screening; these have been used previously with some success; (2) for term 2, calculations of the free–free contribution include e–i collisions in the Born–Mermin approximation (BMA) [89–91] together with local field corrections (LFC) [92, 93] which has been applied with good success to describe the dispersion [42] and width of plasmons [36]. These models show little effect for calculations of the Compton profile which can be tested by comparison with the random phase approximation (RPA) [94]; (3) for term 3, calculations of the bound-free contribution include the form factor approximation and the impulse approximation [84] that show differences for low-temperature HED plasmas with little ionization and which are presently under scrutiny for testing of continuum lowering models. Importantly, the present models include different continuum lowering physics and finite temperature effects.

LCLS provides new opportunities to develop novel physics areas using x-ray scattering. Among those are first-principal electron temperature measurements using detailed balance, observations of plasmon damping by collisions, LFC effects on the plasmon dispersion and effects of viscosity and damping on phonon modes on the ion feature. For high-pressure conditions, elastic and inelastic bound-free scattering can become important and will be utilized in a novel way to characterize ultrafast phase transitions, continuum lowering or ion–ion correlations.

3.2.2. Compton scattering feature. Initially, XRTS was developed in isochorically-heated matter. This path was chosen because the advantage of *a priori* known mass density allows the electron density to be directly inferred from the degree of ionization. The first experiments have tested calculations of the Compton scattering feature that shows significant broadening due to the thermal motion of the electrons resulting in factor of >2 larger width than scattering spectra from cold beryllium [35]. In many dynamic compression experiments, the conditions are close to the Fermi degenerate state. Here, the total width of the Compton peak depends on $\sqrt{E_{Fermi}} \sim {n_e}^{1/3}$ in the partly Fermi degenerate regime with $E_{Fermi} = \hbar^2(3\pi^2 n_e)^{2/3}/2m_e$. Thus, the width of the Compton scattering profile is fairly insentitive to the electron density increase during shock collision. Figure 15 shows an example for 8.5 keV x-ray probing. The challenge will be observing the whole scattering spectrum with sufficient energy range and sufficient resolution to measure this effect.

Finally, with experiments aimed towards producing high-temperature states, Compton scattering is the technique of choice to measure the transition from a Fermi parabolic distribution towards a Boltzmann Gaussian profile whose width provides the electron temperature with high accuracy.

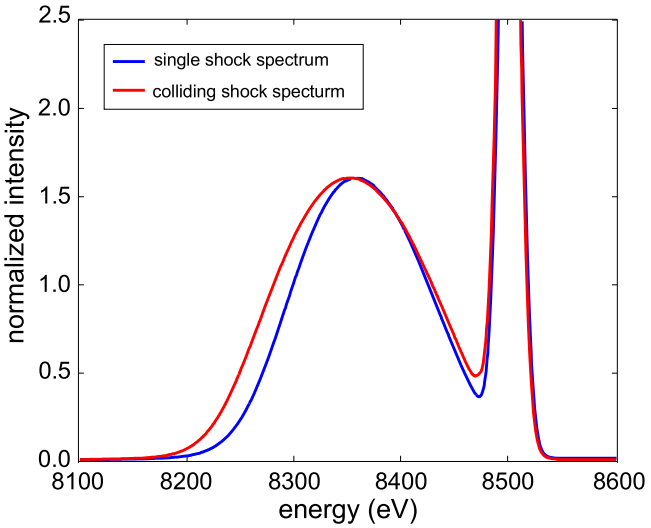

Figure 15. Calculated x-ray scattering spectra for 90° scattering of a 8.5 keV x-ray beam from a aluminum that is shocked by a single strong shock (red curve) or by two counter propagating shock waves (blue curve) with density determined by equation (6).

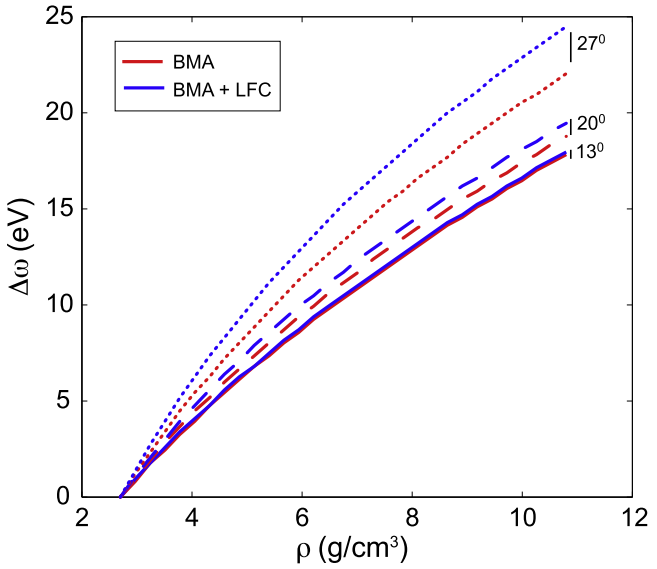

Figure 16. Calculations of the plasmon frequency shift are shown for compressed aluminium and for three scattering angles, temperature of 1.75 eV, and three delocalized electrons. Calculations in the Born–Mermin approximation with and without local field correction agree for a small scattering angle of 13°.

3.2.3. Plasmon scattering. To access collective scattering requires that the scattering parameter must be larger than one:

$$\alpha = \frac{1}{k\lambda_S} = \frac{\text{Scattering length}}{\text{Screening length}} > 1. \tag{9}$$

The scattering length is defined by the scattering vector **k** (equation (7)) and is given by the probe energy and scattering angle: $\lambda = \lambda_0/[4\pi \sin(\theta/2)]$. In the limits of degenerate or classical plasmas the screening length assumes the Thomas–Fermi length or the Debye length, respectively. In case of $\alpha < 1$, the probe radiation with wavelength λ_0 is scattered from electron density fluctuations on a spatial scale λ smaller than the screening length λ_s. In this case, no collective effects like electron plasma oscillations can be observed and the scattered radiation shows the Compton scattering feature providing the electron velocity distribution function. In case of $\alpha > 1$, the scattering wavelength λ is larger than the screening length λ_s. In a weakly degenerate solid-density plasma with an electron temperature of the order of the Fermi temperature, $T_e \sim T_F = 15\,\text{eV}$, collective scattering will occur in forward scattering geometry with $\theta < 40°$ and x-ray probe energies of $E_0 > 3\,\text{keV}$. In this regime, the scattered spectrum shows collective effects corresponding to scattering resonances from electron plasma (Langmuir) oscillation, i.e., plasmons, and from ion-acoustic modes.

In this study, our measurements observe a plasmon shift of $\Delta E = 25\,\text{eV}$ that is approximated by the dispersion relation for plasmons in dense matter, often expressed in the familiar expression [95, 96]:

$$\omega^2 \sim \omega_{pe}^2 + 3(k v_{th})^2 + \left[\frac{\hbar k^2}{2m_e}\right]^2. \tag{10}$$

For HED states, the first term of equation (10) dominates the frequency shift. With ${\omega_{pe}}^2 = n_e e^2/\varepsilon_0 m_e$ the first term being sensitive to the electron density, n_e. The second term is known as the thermal correction from the Bohm–Gross dispersion relation and is of order <5% of the total shift. However, T_e will influence the damping of the plasmon and a rough estimate can be inferred from the fit to the width of the experimental data. The third term is the well-known Compton shift and exactly calculated with equation (1). Higher order terms have been estimated analytically; they are included in numerical results of e.g., [96].

Under the assumption that inter particle interactions are weak, so that the nonlinear interactions between different density fluctuations are negligible, the plasmon shift has been first calculated in the RPA. In the classical limit, it reduces to the usual Vlasov equation. In the limit of the RPA, strong coupling effects are not accounted for, thus limiting the model validity. To expand the theoretical modeling into the WDM regime, the BMA has been developed. The theory was subsequently improved to allow for different models for the dynamic collision frequency and for LFC. Its application to laser experiments on compressed boron has shown that the description of the plasmon dispersion is greatly improved with this theory [42]. However, at the time of this writing, the theoretical description of many-body effects in WDM is not complete.

Figure 16 demonstrates that for small forward scattering angles the calculated plasmon energy shift is not sensitive to the choice of the model for $S_{ee}(k, \omega)$. For a scattering angle of 13° the plasmon shift calculated with BMA and BMA–LFC agree over a range of densities. The shift reflects the relative

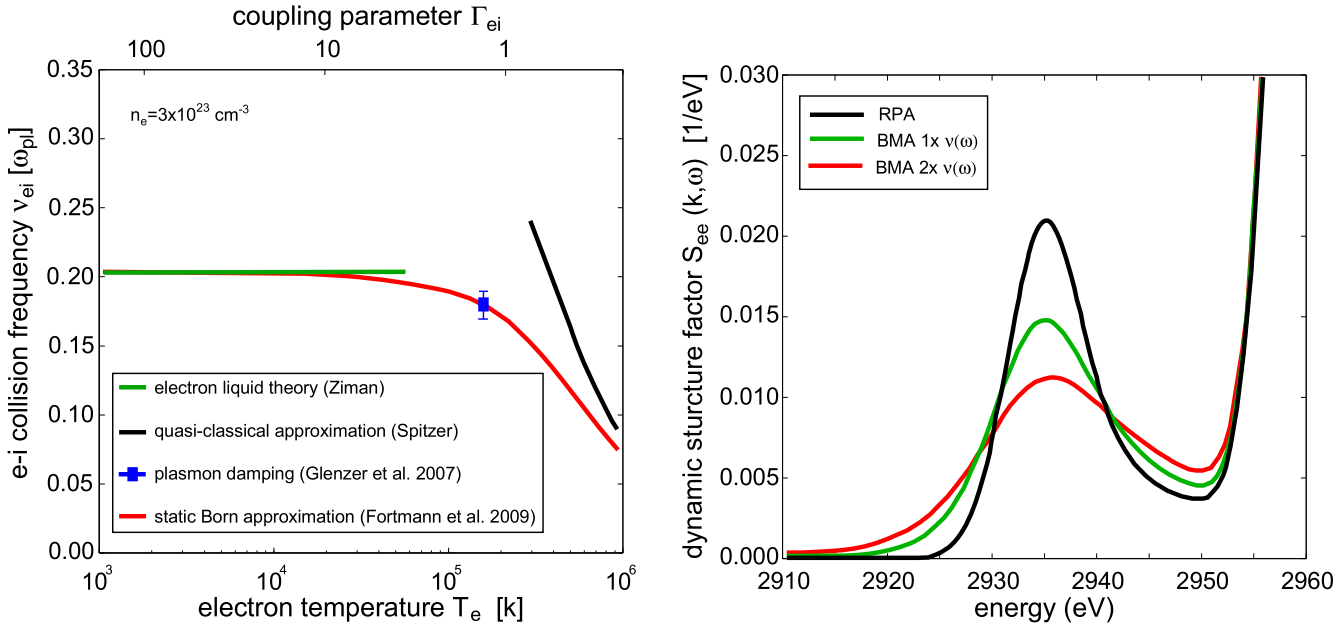

Figure 17. (Left) Electron–ion collision frequency is shown as function of the electron temperature. Previous data inferred from the plasmon measurement [36] compare well with the Born approximation [101]. To validate the theory, future experiments at LCLS will require an independent temperature measurement. (Right) The plasmon width increases significantly with increasing collision frequency.

increase in plasma frequency with density and is well understood compared to the absolute plasmon energy at arbitrary wavenumber. This is apparent in the calculations with increasing scattering angle that show discrepancies between these models. It becomes clear that MEC provides a great opportunity for future investigations of these and related phenomena when using larger scattering angles. For the purpose of the present analysis we conclude that it is possible to achieve an error in density of 5% when choosing conditions where differences in the theoretical approximations are minimized.

3.2.4. Detailed balance. For HED matter at significant temperature, the collective x-ray forward scattering spectrum will show two plasmon features. In addition to the downshifted feature, an up-shifted plasmon will occur on the high-energy wing with nearly the same frequency shift. Compared to the intensity of the downshifted plasmon, the up-shifted intensity is reduced by the Bose–Einstein function dictated by the principle of detailed balance. The intensity ratio of these plasmon features thus offers a first-principal method to measure the ultrafast electron temperature evolution of HED plasmas.

The relation that demonstrates this method is derived from the fluctuation–dissipation theorem. The density fluctuations in the plasma, described by the dynamic structure factor, are related to the dissipation of energy, described by the dielectric function $\varepsilon(\mathbf{k}, \omega)$

$$S(\mathbf{k}, \omega) = \frac{\varepsilon_0 \hbar k^2}{\pi e^2 n_e} \frac{\mathrm{Im}(\varepsilon^{-1}(\mathbf{k}, \omega))}{1 - \exp(\hbar\omega / k_B T_e)}. \quad (11)$$

Independent of evaluating the dielectric function, the shape of the structure factor, and modeling collisional effects, the dielectric function fulfills the requirement

$$\frac{S(\mathbf{k}, \omega)}{S(-\mathbf{k}, -\omega)} = \mathrm{e}^{-\hbar\omega / k_B T_e}. \quad (12)$$

This relation is referred to as the detailed balance relation. As a general consequence, the structure factor shows an asymmetry with respect to $\mathbf{k}$ and ω. When applied to plasmons, it provides the electron temperature independent of a detailed formulation of dissipative processes in the plasma. In past laser experiments, due to small signal-to-noise ratios limited information was obtained on T_e [36, 97], making a future systematic studies with small noise amplitudes highly interesting.

3.2.5. Collisions. The width of the plasmon feature is sensitive to collisions, thus providing a measurement of the e–i collision frequency and consequently a novel method for measuring conductivity and equilibration. Figure 17 shows the comparison between measured and calculated collision frequency ν_{ei} and sensitivity of the plasmon width to ν_{ei}. From the e–i collision rate the conductivity can be inferred through the Ziman formalism [98, 99]. This can readily be seen from the dependence of the x-ray scattering spectrum on the dielectric function $\varepsilon(\mathbf{k}, \omega)$. The generalized expression for the dielectric function in the Mermin approximation employs the standard collision-less value obtained in the

RPA, $\varepsilon^{\mathrm{RPA}}(\mathbf{k}, \omega)$, and the collision frequency $\nu(\omega)$

$$\varepsilon^{\mathrm{M}}(\mathbf{k}, \omega) = f(\varepsilon^{\mathrm{RPA}}(\mathbf{k}, \omega + \mathrm{i}\nu(\omega)), \varepsilon^{\mathrm{RPA}}(\mathbf{k}, \omega), \nu(\omega)). \quad (13)$$

The collision frequency obtained in this way is related to the conductivity through the plasma coupling parameter Γ [100]

$$\sigma(\omega) = \lambda(\Gamma)\frac{e^2 n_{\mathrm{e}}}{m_{\mathrm{e}}\nu(\omega)} \text{and } \Gamma = \frac{e^2}{kT_{\mathrm{e}}}(4\pi n_{\mathrm{i}}/3)^{1/3}. \quad (14)$$

Thus, measurements of the plasmon spectrum have the potential to provide critically important information on equilibration and hydrodynamics but must use high spectral resolution and high signal-to-noise detection unique to LCLS.

3.2.6. The ion feature. LCLS high photon flux of narrowband and coherent x-rays are now available to study the dynamics of the low-frequency correlations (the ion-acoustic waves). The dispersion curve of and the details of ion correlations have long remained elusive in the HED physics regime [82, 88], with almost no comparison with experimental data except for the case of liquid metals at room temperature [102]. New studies at LCLS will be able to investigate contributions of LFC and the relevance of hydrodynamics and generalized hydrodynamics formulations on plasma transport properties [103, 104]. Further, predictions for additional dispersion at large wave numbers can be tested [63, 105].

Of particular interest are pump–probe experiments where unequal electron and ion temperatures will be produced. Thus, the measurement of the ion acoustic resonances will provide a direct estimate of the ion temperature, while the measurement of plasmon resonances will give the electron temperature. This platform can provide new insights in the e–i coupling in HED experiments at MEC.

3.2.7. Ion–ion correlations. Unique to LCLS MEC is the fact that one can further develop x-ray scattering diagnostic to simultaneously resolve both the spectral and angular (**k**-vector) components of the XRTS signal during a dynamic laser and x-ray heating experiment. In particular, when significant compression occurs, for example due to strong shock waves, accurate measurements can be achieved. The momentum-resolution of such methods has not previously been achieved in WDM research and is critically needed to measure the material structure in conditions with simultaneous spectrally-resolved scattering measurements. Such experiments will take advantage of the strong correlation peaks in the scattering intensity of the elastic scattering component (1st term of equation (8)).

The ionic structure factor peak has been observed recently for the first time in shock-compressed aluminum. In these experiments, aluminum was shocked from one side [46] and data were accumulated over 3 separate shot days at the Omega laser [45]. The absolute strength of the scattering amplitude and overall predicted shape have shown that HNC calculations with repulsive potentials and SOCP models provide an improved description while Debye–Hückl screening models show weaker correlations and smaller scattering amplitudes than the experimental data.

For matter with strong ion–ion correlations the frequency integral of equation (8), $S^{\mathrm{total}}(\mathbf{k})$, is given by the Fourier transform of the pair–correlation function $g(\mathbf{r})$:

$$S^{\mathrm{total}}(\mathbf{k}) = 1 - n\int \mathrm{d}^3\mathbf{r}\,\exp(-\mathrm{i}\mathbf{k}\mathbf{r})[g(\mathbf{r}) - 1] \quad (15)$$

with

$$\mathrm{g}(\mathbf{r}) = \frac{1}{Nn}\int \mathrm{d}^3\mathbf{r}'\, n(\mathbf{r} + \mathbf{r}')n(\mathbf{r}'), \quad (16)$$

where n is the average density, N is the number of particles in the scattering volume. Hence, $S^{\mathrm{total}}(k)$ is a direct measure of pair correlations in dense matter. Equations (15) and (16) predict a shift of the calculated maximum elastic x-ray scattering amplitudes to higher wave number with increased density. For higher densities, the mean separation between ions decreases providing scattering peaks at larger scattering angles and thus larger wave number **k**. Here, the small **k**-vector spread of the incoming LCLS beam is required to resolve the shift of the structure peak. Importantly, different theoretical models of the ion–ion correlation predict differences in the widths, which have been resolved in experiments at MEC and which are discussed further below.

3.3. DFT-MD simulations

DFT-MD simulations of this study were performed for a range of temperature and density conditions [61–63] spanning the experimental parameters accessible by the MEC laser capabilities. The primary goals were to calculate the ion–ion correlation feature and to determine the material physical properties. Here, the core radius is $r_{\mathrm{C}} = 1.7a_{\mathrm{B}}$ with $a_{\mathrm{B}} = 0.53$ Å. The Mermin functional accounts for thermal excitations. The electronic cut off for the plane wave representation of the wave function is set to 550 eV as tested to provide the free energy and pressure with about 0.7% accuracy.

The simulations have been performed in a super-cell with constant number of particles, volume and temperature with periodic boundary conditions. A total of $N = 256$ ions have been used for the fluid. Initial runs have been performed at lower temperatures starting with the ions in an fcc lattice at the appropriate densities of the experiment. The resulting ionic configurations were then used as starting configurations for runs at the temperatures of interest. The simulations run for 2000–23 000 steps with a 0.2 fs time step. An initial relaxation time of varying length was excluded from the analysis of the EoS.

Figure 18 shows results from DFT-MD simulations of the total x-ray scattering amplitude versus scattering vector **k** for WDM conditions. These simulations show a well distinguished peak and determine temperature and density sensitivity of the angularly-resolved scattering measurements.

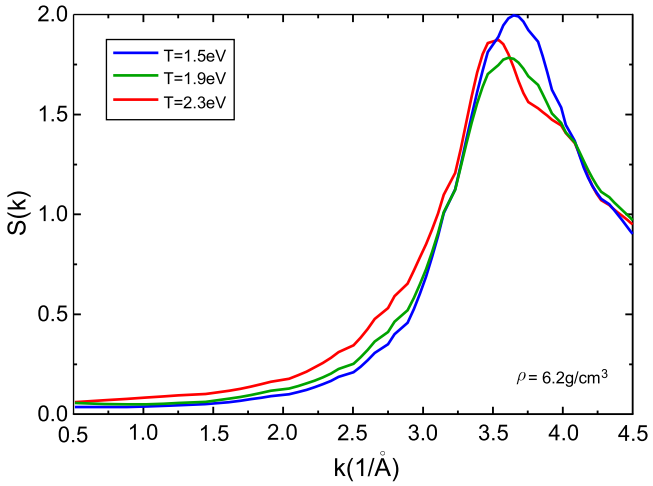

Figure 18. The total x-ray scattering amplitude is shown as function of the wave number **k** for compressed matter states. Calculations for various temperatures ($T_e = T_i$) show that the width of the correlation peak increases with increasing temperatures. Also, the absolute peak amplitude is sensitive to temperature.

4. Results and discussions

4.1. Shock compressed matter

4.1.1. Experimental results. Figure 19 shows the schematic of dynamically compressed matter experiments at MEC. Also shown are data records from the x-ray scattering detectors. The spectrometers have been fielded for density and temperature measurements from plasmons and angular resolved scattering provides diffraction and structure factor data. Here, two 4.5 J laser beams irradiate 50 μm thick Al foils (initial density of $\rho_0 = 2.7\,\mathrm{g\,cm^{-3}}$) that are coated with 2 μm thick parylene. The laser beams are absorbed in the parylene, heat the material and launch two counter-propagating multi-megabar shock waves into the solid aluminium by ablation pressure. For the conditions achieved in this experiment, we find that the shocks propagate inward at $14\,\mathrm{km\,s^{-1}}$, each shock wave compressing the aluminium target to about $5\,\mathrm{g\,cm^{-3}}$.

The shock speed and planarity over the central 10 μm diameter region were verified by shock breakout measurements from 25 μm thick foils irradiated by a single beam. Thus, when adding the second beam on the opposite side of the target, we doubled the foil thickness to 50 μm to mirror the shock propagation. Figure 20 shows that the averaged shock velocity varies by <2% over the region probed by the x-ray beam. Also, the shock velocity is seen to scale with laser intensity for two different focal spot sizes. When the shocks coalesce in the center of the foil, the density is expected to significantly increase to about $7.5\,\mathrm{cc^{-1}}$ reaching peak pressures of 5 Mbar.

In this study, accurate measurements of compression have been achieved by measurements of the electron plasma (Langmuir) oscillations. These measurements test the predictions of compression based on equations (1)–(6) by applying the theory of equations (8) and (10). Figure 21 shows the plasmon scattering spectra and theoretical fits of the dynamic structure factor $S(\mathbf{k}, \omega)$ near peak-compression at $t = 1.9$ ns. These data are compared with measurements from uncompressed aluminium. The plasmon feature is downshifted from the incident 8 keV x rays as determined by the generalized Bohm–Gross dispersion relation, see equation (10), and its resonance frequency is used as a sensitive marker of the electron density, see figure 16. While the data from uncompressed aluminium yield a total plasmon shift of 19 eV providing a free electron density of $1.8 \times 10^{23}\,\mathrm{cm^{-3}}$ the total shift increases to 29 eV at shock coalescence. For the example shown in figure 21, a density of $4.1 \times 10^{23}\,\mathrm{cm^{-3}}$ has been measured and corresponding to 2.3× compression. The error in electron density is ±5% determined by noise in the data and the fit of the theoretical dynamic structure factor.

The maximum density measured at shock coalescence is $7\,\mathrm{g\,cc^{-1}}$ slightly less than expected from estimates discussed above. Specifically, we find that compression in the first shock is slightly lower than predicted due to varying total peak powers and probably also due to the slow rise time of the laser pulse. Typical values are $1.2 < \rho_1/\rho_0 < 1.9$, which when combined with the compression due to coalescence of $\rho_2/\rho_1 \sim 5/3$ results in final compression values of $\rho_2/\rho_0 > 2$.

The scattering spectra further provide a measure of the temperature by analyzing the intensity of the elastic scattering features. For this purpose, structure factors are determined from wavenumber resolved scattering while the absolute intensity is determined by the intensity ratio with the plasmon feature; the plasmon intensity is determined by the *f*-sum rule (particle conservation)

$$\int_{-\infty}^{\infty} \left(\frac{\mathrm{d}^2\sigma}{\mathrm{d}\Omega \mathrm{d}\omega}\right)_{\mathrm{Plasmon}} \omega \mathrm{d}\omega = \frac{Z\hbar k^2}{2m_e}, \qquad (17)$$

where $(\mathrm{d}^2\sigma/\mathrm{d}\Omega\ \mathrm{d}\omega)_{\mathrm{Plasmon}}$ is the measured plasmon intensity from the free electron Langmuir oscillations. Here, $Z = 3$ is the ion charge state, $\hbar$ is Planck's constant, k is the wavenumber and m_e the electron mass. At peak compression, the intensity of the elastic scattering feature increases by a factor of 2.8 over the cold scattering amplitude. We use a model [84] to fit the measured intensities; the potential and structure factors are shown in section 4.1.2; they are in excellent agreement with the experimental data and DFT-MD simulations, see figure 18. For the example shown in figure 21 the temperature is $T = 20\,000$ K, i.e., 1.75 eV ± 0.5 eV. For our conditions, the ultrafast x-ray pulse deposits 3500 K or 0.3 eV per electron into the target. A fraction of the energy can be expected to heat the electron fluid, but the total energy is small compared to shock heating and will not affect the plasmon shift. In addition, within the duration of the x-ray pulse, the ionic correlations have no time to respond to changes of the screening properties as demonstrated by the observation of solid and solid compressed states of aluminium.

Figure 22 shows the wavenumber resolved scattering data from which we obtain the high-pressure ion–ion structure factors. At $t = 0$, before the rise of the optical laser beam

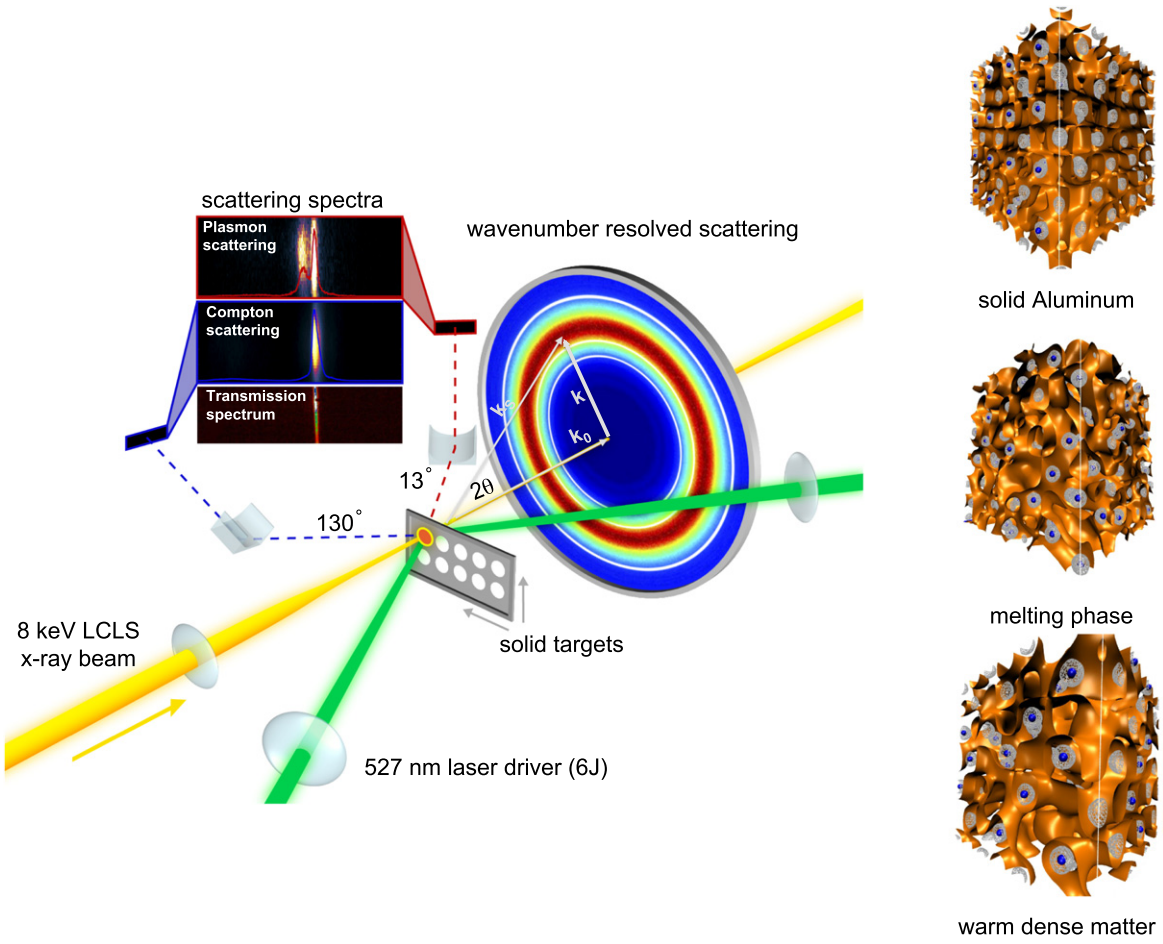

Figure 19. (Left) A schematic of experimental setup for compressed matter studies at MEC is shown. The LCLS x-ray beam is focused into the dense laser-compressed aluminium target. The 13° forward x-ray scattering spectrum shows inelastic plasmon scattering together with the elastic scattering feature at the incident x-ray energy. The 130° backscattering shows no scattering feature in this energy range validating the identification of the plasmon. A CSPAD area detector observes the total wavenumber-resolved x-ray scattered intensity indicating the transition from Debye–Scherrer diffraction rings (white) to an intense ion–ion correlation scattering feature (red). (Right) DFT-MD simulations of the formation of WDM indicate that the ions (blue) abandon their lattice positions. Whilst core electrons (gray) remain mostly unchanged the delocalized conduction electrons (represented by orange iso-surfaces) are disturbed from the very regular structure in the lattice.

power, the data show peaks from Debye–Scherrer rings indicating the ionic lattice in the solid. The peaks at 38°, 45°, and 65° correspond to (111), (200), and (220), respectively. When the shocks are launched and compress the solid, the lattice spacing d is reduced and we observe that the peaks shift to larger scattering angles as determined by the Bragg scattering equation $n\lambda_{\text{x-ray}} = 2d\ \sin\theta$, here $\lambda_{\text{x-ray}} = 1.55$ Å the wavelength of the incident x-ray laser, and 2θ the scattering angle.

With increasing pressures, the aluminium melts and transitions into the WDM state. We first observe a comparatively broad ion–ion correlation peak at an angle of 45° at 1.38× compression together with shifted Bragg scattering of solid compressed aluminium. For these conditions the comparison with simulations shows that the wave number of both the ion–ion correlation peak and the shifted Bragg peak provide the same density indicating a co-existence regime. With higher pressure accessed later in time and with higher laser intensity, we compress aluminium up to 1.9× the initial density and the strong ion–ion correlation peak shifts to $2\theta = 51°$. At shock coalescence, the peak shifts further to $2\theta = 55°$ and the data indicate 2.3× compressed aluminium consistent with densities inferred from the simultaneous measurements of the plasmon shift.

The measured ion–ion correlation feature is sensitive to the ion–ion structure factor, see equation (8). For nearly elastic scattering the scattering angle 2θ determines the wavenumber of the correlations. With $\boldsymbol{k} = 2\boldsymbol{k}_{\text{x-ray}}\ \sin\theta$ and $k = 2\pi/\lambda$ determining the scale length of the density fluctuations measured in this scattering experiment, we find 1.38 Å $< \lambda_{\text{SL}} <$ 5.7 Å. On these atomic scale lengths, the scattering amplitude is probing important details of the ion–ion interaction potential V_{ii}.

4.1.2. Physical properties. For the analysis of the measured scattering data and the ion–ion correlation feature various theoretical approximations have been considered. The data depend on both material compression, temperature, and on the

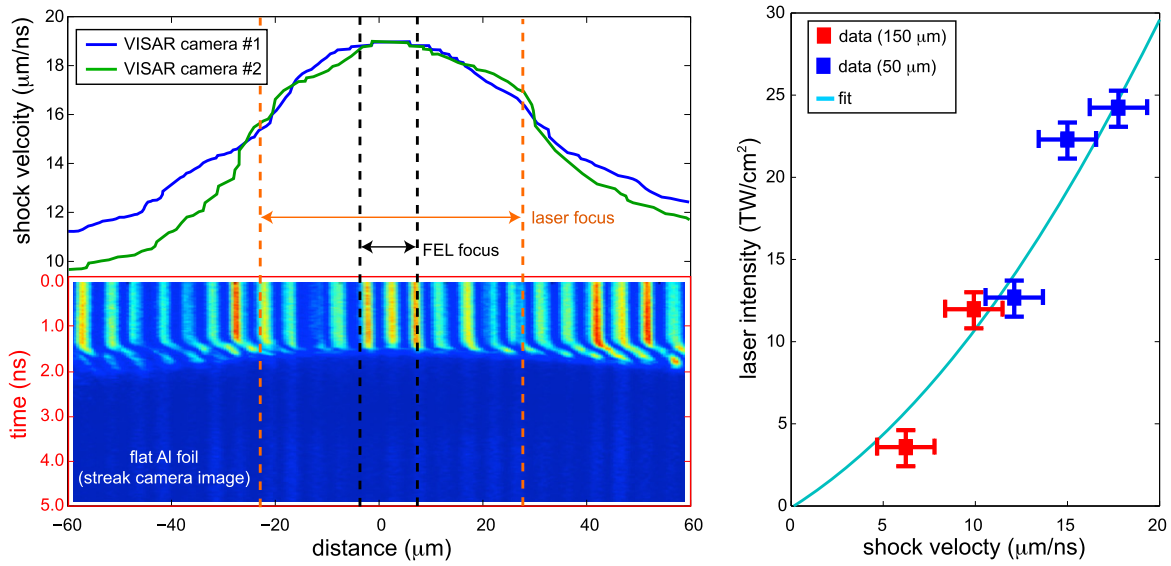

Figure 20. (Left) Results from shock breakout measurement from flat aluminium foils. The averaged shock velocity planarity is <2% in the central region probed by the LCLS x-ray beam. (Middle) An example of a VISAR streak camera record is shown from laser-driven aluminium. (Right) The averaged shock velocity is plotted for various laser intensities using two different phase plates with 50 μm and 150 μm spot size.

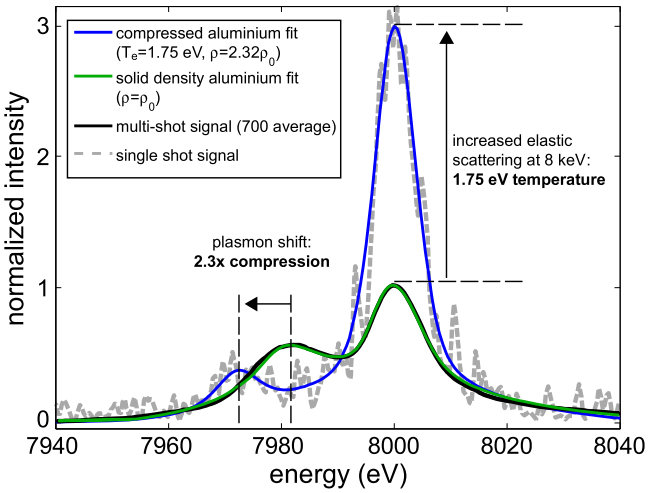

Figure 21. X-ray scattering spectra from compressed and solid-density aluminium are shown. A significant increase in plasmon frequency shift and elastic Rayleigh scattering amplitude occurs with compression. The experimental data (black and gray dashed curves) are fitted with theoretical dynamic structure factor (equation (8)) calculations (light straight curves). The elastic scattering amplitude provides the temperature of 1.75 eV. The plasmon shift $\hbar\omega$ is primarily determined by the increase in plasma frequency measuring the electron density. In this example, the plasmon shift indicates material compression of 2.3 times solid density with $\rho = 6.3$ g cc^{-1}.

choice of the many particle theory to describe the interaction physics. Here, densities and temperatures are inferred from the plasmon scattering spectra providing an excellent experimental test of theory and simulations by comparing predictions with the measured wavenumber-resolved scattering data. In previous studies, the measurements of the elastic scattering amplitude alone was often not sufficient to provide information about the state of the dense plasma. This is due to the fact that calculations of $S_{ii}(k)$, e.g., using the HNC approximation, must assume an effective interaction potential. In this study, $S_{ii}(k)$ is directly obtained from the measured wavenumber resolved scattering data using $W(k) = S_{ii}(k)(f(k) + q(k))^2$ with the atomic form factor $f(k)$ and the screening function $q(k)$ calculated from the number of bound core electrons, $Z_C = 10$ for aluminium.

Figure 23 shows various screening functions $q(k)$ and atomic form factors $f(k)$. Combining these results with our measurements of the wavenumber resolved scattering data, $W(k)$, demonstrates the sensitivity of the choice of the function $q(k)$. HNC calculations with a screened Coulomb potential using a Yukawa screening term (Y) together with a SRR term provide excellent agreement with the measured data. This is illustrated as the full curves in figure 22 that agree with both experiment and the results from the DFT-MD simulations. Similar results can be obtained with a hard sphere model. However, it is apparent that a Coulomb potential or a screened Coulomb potential cannot account for the experimental observations, see dashed curves in figure 22. At small wavenumbers, we note that these models show different sensitivity to the temperature. This is due to the fact that the repulsive core part of the potential is temperature independent; the remaining sensitivity is due to the temperature dependence of the screening cloud. Here, DFT-MD simulations shown in figure 18 provide the temperature dependence that is applied for the interpretation of the elastic scattreing amplitude in the plasmon spectra, see figure 21. The error in temperature can be estimated to be in the range of 0.5 eV–0.7 eV including contributions from both uncertainties in the models and noise of the data.

The analysis presented in figures 22 and 23 provide the following physical picture for the ion–ion structure factor in WDM: by matching the pair correlation functions $g(r)$, the

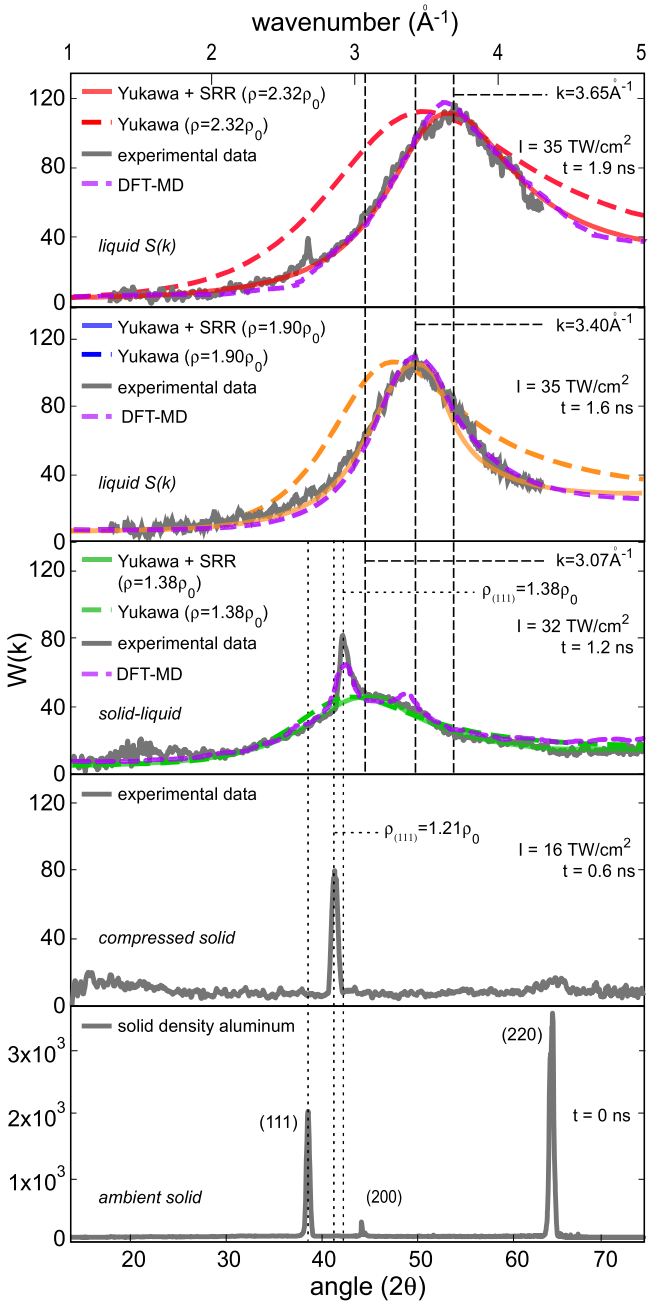

Figure 22. X-ray scattering data $W(k)$ are shown as function of scattering angle. (Bottom) Bragg peaks from Debye–Scherrer rings are shown at $t = 0$ ns. (2nd from bottom) Data from compressed solid aluminium show a shift of the (111) Bragg peak by 3° and compression of 1.21 ρ_0. (Middle) Appearance of a broad ion–ion correlation peak is observed together with a Bragg peak shifted further to larger angles. (2nd from top) At higher compression, aluminium melts, Bragg peaks disappear, and the ion–ion correlation peak shifts to 50°. (Top) The angle of the correlation peak increases further to 56° when higher densities are reached after coalescence. The data (black curves) show excellent agreement with DFT-MD simulations (top three panels). The data can also be described by a model that accounts for both screening and short-range repulsion (red, blue and green solid curves), but a screened potential alone is not sufficient (dashed curves).

effective ion–ion pair potentials can be directly extracted from the DFT-MD simulations that show the importance of including both SSR and screening. The interaction potential

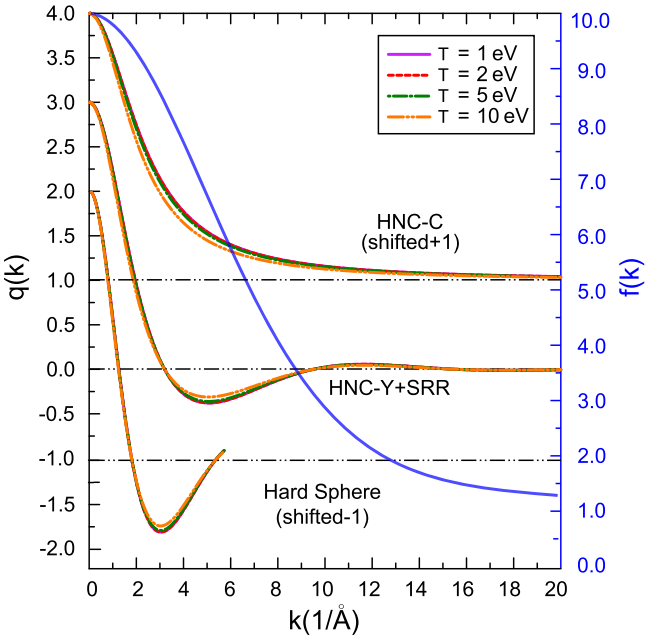

Figure 23. Three screening functions $q(k)$ are shown for temperatures ranging from 1 eV to 10 eV along with the atomic form factor $f(k)$. While HNC-Y + SRR and hard sphere models agree well with the data, models that only include screening provide a poor match with the data.

can be described as

$$\beta V_{\mathrm{ii}}(r) = \frac{Z^2 e^2}{r k_{\mathrm{B}} T} \mathrm{e}^{-\kappa r} + \frac{\sigma^4}{r^4}, \tag{18}$$

with r being the distance between ions, k_{B} is Boltzmann's constant, e the electron charge number. The exponent $\kappa = \kappa(n_{\mathrm{e}}, T_{\mathrm{e}})$ is the Yukawa screening function. For our conditions, κ approaches the Thomas–Fermi screening length with accuracy of better than 1%. The last term in equation (19) accounts for the additional repulsion from overlapping bound electron wave functions, with the parameter σ fitted to match DFT-MD simulations [59]. Figure 22 (top three panels) shows that the DFT-MD simulations, results based on equation (18), and the wavenumber resolved scattering data agree well with each other for densities obtained independently from the plasmon or Bragg scattering data. Importantly, linearly screened Coulomb potentials, denoted here by Yukawa in figure 22, show no agreement with the experimental data.

The data and simulations can further be used to describe the angle of the maximum scattering amplitude; the latter is sensitive to the density. Figure 24 compares the angle of maximum scattering amplitude with the density from the plasmon x-ray scattering data. Also shown are various theoretical approximations. The result show that using equation (18) for the calculation of the dynamic structure factor $S(k, \omega)$ provides a model to determine density from wavenumber resolved scattering.

The therory and simulations can now be applied to analyze the scattering data for potential gradients in the x-ray

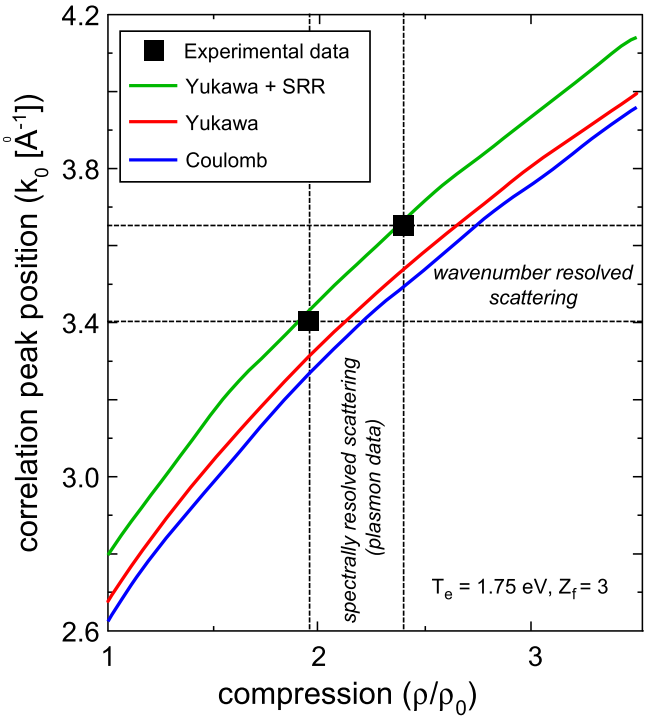

Figure 24. The measured wavenumber of the ion–ion correlation peak that is reflected by the maximum x-ray scattering amplitude is shown versus compression from plasmons (error bars are of the size of the symbols). The comparison with theory shows that including short-range repulsion correctly predicts the scattering angle.

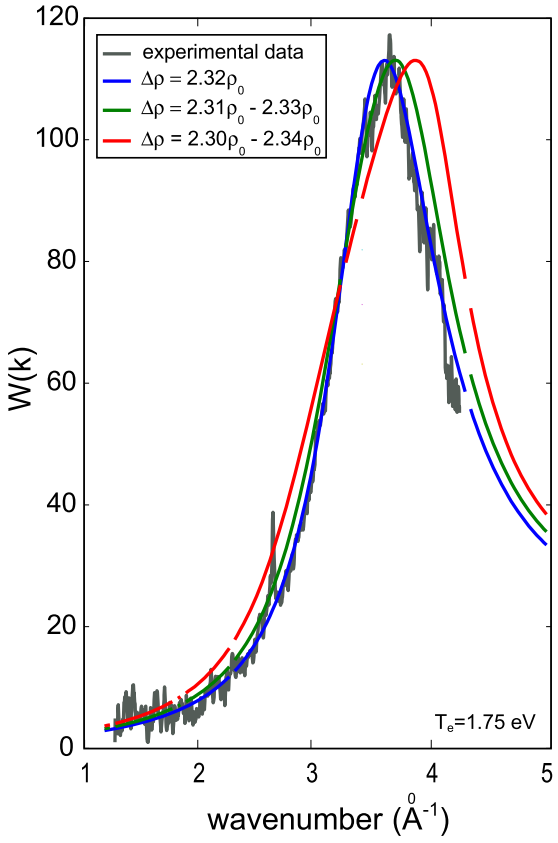

Figure 25. The wavenumber resolved scattering data $W(k)$ are compared with calculations of the ion–ion correlation functions. The latter represents the sum of scattering results calculated for a range of density values and combined to an effective synthetic scattering result. This analysis indicates that density gradients are less than 5%; larger values result in a width of the correlation peak not consistent with the experimental results.

probing region. Potential non-uniform shock conditions could give rise to different conditions either transversly over the 10 μm x-ray probe cross section or along the shock propagation direction. Clearly, the latter will always include the low density blow-off plasma and if probed early in time the unshocked material ahead of the shock. However, the x-ray scattering amplitude is weighted towards the highest density and the broad ion–ion correlation feature can only be observed after shock melting. To quantitativly estimate the effect of gradients the wavenumber resolved scattering can be compared with calculations for the ion–ion structure factor for a range of density conditions.

Figure 25 shows the x-ray scattering data together with calculations for a density of $\rho = 2.32\ \rho_0 \pm \Delta\rho$. The density range is assumed to be linear over the ranges indicated in the figure. The results indicate that density gradients are negligibly small for the present experimental conditions and are less than 5%.

Finally, the experimental and theoretical structure factors further provide a new method for determining the material pressures. In particular, the measured wavenumber resolved scattering data $W(\mathbf{k})$ yield the structure factor $S(\mathbf{k})$ using $W(k) = S(k)[f(k) + q(k)]^2$ with the atomic form factor $f(k)$ and the screening function $q(k)$ that can be integrated and which provides a novel method for determining the pressure [106]. The total pressure consists of ionic and electronic contributions with $P_{\rm tot} = P_{\rm i} + P_{\rm e}$. In nearly Fermi degenerate conditions, $P_{\rm e}$ includes well-known density-sensitive contributions accounting for Fermi pressure, degeneracy, Coulomb, and exchange terms. On the other hand, the ion pressure, when divided into an ideal gas part $P_{\rm G} = n_{\rm i} k_{\rm B} T$ and the correlation part $P_{\rm i} = p^x + P_{\rm G}$, is dominated by the (negative) ion excess pressure

$$p^x = \frac{n_{\rm i} U}{3N} - \frac{n_{\rm i}(Ze)^2}{12\pi^2}\int_0^\infty S(\mathbf{k})\frac{\kappa^4}{(k^2+\kappa^2)^2}\mathrm{d}\mathbf{k} \qquad (19)$$

with U/N being the internal energy. In equation (19), the structure factor directly obtained from the measured wavenumber resolved scattering data can be used.

Figure 26 compares the experimental pressure data [22] with available empirical data [107] and state-of-the-art simulations. In particular, we show previous DFT-MD simulations for temperatures calculated for the shock Hugoniot [62] together with our DFT-MD simulations performed for temperatures and densities of the present experiment [61]; the simulations provide excellent agreement with the data from the experiment. The data further show no indication of Bragg peaks for compressed aluminium above $P = 1.2$ Mbar consistent with previous melt line measurements on the Hugoniot [108]. The present data set extends further showing the disappearance of Bragg scattering data above 1.2 Mbar and up to densities of 4.5 g cc^{-1}. At higher

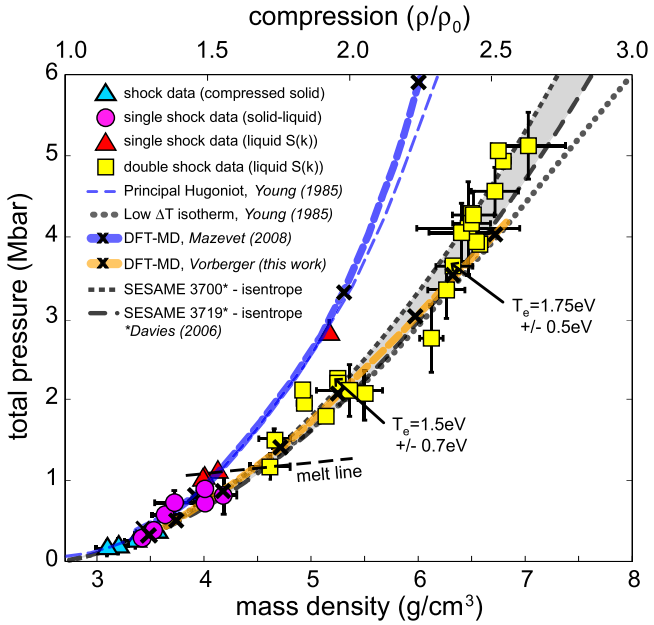

Figure 26. The comparison of pressure data of compressed dense aluminium measured for varying laser intensity is shown from single shocks and during shock coalescence of two counter-propagating shock waves. The single shock data follow the shock Hugoniot and DFT-MD simulations from $\rho = 3.5$ g cm^{-3} to about $\rho = 4$ g cm^{-3}. In addition, a high-density Hugoniot data point at > 5.2 g cm^{-3} was obtained in single shot targets. When the shock waves coalesce the increase in pressure is nearly adiabatic and is approaching an isentrope to $\rho = 7$ g cm^{-3}. The melt line (dashed) indicates the complete disappearance of shifted Bragg peaks. The DFT-MD simulations show excellent agreement when using the measured density and temperature data.

pressures, the shock coalescence data are on the isentrope [109] slightly above the isotherm [107] validating our understanding of dense aluminium utilizing pressure, temperatures and densities solely based on measurements.

These new experimental and theoretical findings demonstrate that spectrally and wavenumber resolved x-ray scattering is applicable for thorough testing of radiation-hydrodynamic calculations and EoS models. The method presents unique highly resolved data for dynamic high-pressure material science studies that require accurate knowledge of material properties and the thermodynamic state at high densities and are applicable for future studies aimed at observing effects of ionization on the EoS at high compression.

5. Summary and outlook

The first experiments at the MEC instruments have utilized record peak brightness x-ray laser radiation to probe high-power laser-driven targets demonstrating the unique capability to accurately measure the thermodynamic state of dense dynamically compressed matter. In particular, the forward x-ray scattering measurements have resolved the plasmon scattering spectrum providing a highly accurate tool to provide *in situ* measurements of the density and temperature evolution. This capability is accurate enough to test dense plasma theory used in radiation-hydrodynamic modeling and predictions of the physical properties of dense matter. Comparisons of the wavenumber resolved scattering data with DFT and reduced models have revealed the importance of including ion–ion interaction potentials that account for SRR. Differences can be seen between the data and results using orbital free Thomas–Fermi modeling or one component plasma theory. This success indicates that future applications of this technique may allow ultrafast pump–probe studies for measurements of e–i equilibration, heat and radiation transport and the thermodynamic equilibration of matter. Dense plasma effects can be studied with precision measurements of the plasmon dispersion, amplitude and plasmon broadening through Landau and collisional damping processes. Further, future x-ray scattering experiments in the Compton regime may reveal Pauli blocking and test models of continuum lowering.

For these studies, it is important to combine spectrally resolved scattering with angularly resolved scattering and optical velocity interferometer measurements. Here, dynamic x-ray diffraction data have visualized the transitions from a solid, compressed solid, into the co-existence regime, and to a WDM state. The measurements provide structural information of the compressed lattice and further allow inferring pressures in the multi-Mbar regime. We find excellent agreement with DFT-MD simulations on the shock Hugoniot or at shock coalescence using the temperatures and densities of the experiment. These data demonstrate measurements of structural phase transitions, melting curves, shock Hugoniot, and isentropic shock coalescence states. Importantly, larger explorations of the phase space of matter at high pressures will require future combinations of free electron x-ray lasers with higher-energy optical drive lasers. Our studies show that it will be possible to characterize conditions [110–113] found in white dwarfs to help determine the age of galaxies, provide insights into new high-pressure materials [114], and to test theoretical models that are applied for inertial confinement fusion experiments and calculations of the structure and magnetic fields of extrasolar planets.

This rich area of physics will be explored at multiple free electron laser facilities. Currently two hard x-ray free electron lasers are in operation worldwide, LCLS at SLAC in Stanford running since 2009 for users with the MEC instrument available since 2012 and which is the subject of this review. In addition, SACLA is in operation since 2012 at Spring8 in Harima. HED science experiments have recently begun, for example saturable absorption has recently been measured in iron targets using ultrahigh x-ray intensities of 10^{20} W cm^{-2} [115]. Current capabilities already include high-power drive lasers for pump–probe experiments. Two additional free electron lasers are in operation in the extreme ultraviolet and soft x-ray spectral ranges. The first facility to become available was FLASH at DESY in Hamburg, which started operation in 2005 [29–31] where pump–probe capabilities were recently added for HED experiments [32]. FERMI at ELETTRA in Trieste is running since 2012 [116]. MEC is an

active area of research at all four facilities soon to be joined by a fifth instrument at the European XFEL.

In the near future, these facilities will begin exploring a new area for research of MEC by combining short pulse high-power lasers with the high brightness x-ray laser beam. Accurate measurements of density fluctuations using x-ray scattering and phase contrast imaging have the potential to reveal laser-induced collision-less shocks and characterize the nonlinear evolution of Weibel instabilities with the goal to demonstrate the physics of cosmic rays. Further, these techniques are important for measuring density fluctuations in laser-proton acceleration or laser-produced anti-matter studies. Finally, short pulse lasers are itself an excellent source of bright and ultrafast sources of x-rays and energetic particles allowing future ultrafast pump–probe studies with complementary sources to measure the fundamental process in photon–matter interactions.

Acknowledgments

This work was supported by DOE Office of Science, Fusion Energy Science under FWP 100182. The experiments were performed at the Matter at Extreme Conditions (MEC) instrument of LCLS, supported by the DOE Office of Science, Fusion Energy Science under contract No. SF00515. This work was further supported by Laboratory Directed Research and Development grant, the Peter-Paul-Ewald Fellowship of the VolkswagenStiftung, and the Theodor-von-Lynen Fellowship of the Alexander-von-Humboldt foundation.

References

[1] Motz H 1979 *The Physics of Laser Fusion* (London: Academic)
[2] Lindl J D, Amendt P, Berger R L, Glendinning S G, Glenzer S H, Haan S W, Kauffman R L, Landen O L and Suter L J 2004 The physics basis for ignition using indirect-drive targets on the National Ignition Facility *Phys. Plasmas* **11** 339
[3] Lind J D *et al* 2014 Review of the National Ignition Campaign 2009–2012 *Phys. Plasmas* **21** 020501
[4] Glenzer S H *et al* 2012 First implosion experiments with cryogenic thermoniclear fuel on the National Ignition Facility *Plasmas Phys. Control. Fusion* **54** 04013
[5] Atzeni S and Meyerter-Vehn J 2004 *The Physics of Inertial Fusion* (Oxford: Clarendon)
[6] Clayton C E *et al* 2010 Self-guided laser wakefield acceleration beyond 1 GeV using ionization-induced injection *Phys. Rev. Lett.* **105** 105003
[7] Zepf M *et al* 2003 Proton acceleration from high-intensity laser interactions with thin foil targets *Phys. Rev. Lett.* **90** 064801
[8] Kemp A J and Divol L 2012 Interaction physics of multipicosecond petawatt laser pulses with overdense plasma *Phys. Rev. Lett.* **109** 195005
[9] Sentoku Y, d'Humières E, Romangnani L, Audebert P and Fuchs J 2011 Dynamic control over mega-ampere electron currents in metals using ionization-driven resistive magnetic fields *Phys. Rev. Lett.* **107** 135005
[10] Krushelnick K *et al* 2008 Effect of relativistic plasma on extreme-ultraviolet harmonic emission from intense laser-matter interactions *Phys. Rev. Lett.* **100** 125005
[11] Hegelich B M *et al* 2006 Laser acceleration of quasi-monoenergetic MeV ion beams *Nature* **439** 441–4
[12] Blandford R and Eichler D 1987 Particle acceleration at astrophysical shocks: a theory of cosmic ray origin *Phys. Rep.* **154** 1–75
[13] Kugland N L *et al* 2012 Self-organized electromagnetic field structures in laser-produced counter-streaming plasmas *Nat. Phys.* **8** 809–12
[14] Guillot T 1999 Interiors of giant planets inside end outside the solar system *Science* **286** 72
[15] Nettelmann N, Holst B, Kietzmann A, French M, Redmer R and Blaschke D 2008 *Ab initio* equation of state data for hydrogen, helium, and water and the internal structure of Jupiter *Astrophys. J.* **683** 1217
[16] Ross M 1981 The ice layer in uranus and neptune—diamonds in the sky? *Nature* **292** 435
[17] Coppari F *et al* 2013 Experimental evidence for a phase transition in magnesium oxide at exoplanet pressures *Nat. Geosci.* **6** 926–9
[18] Fiuza F, Fonseca R A, Tonge J, Mori W B and Silva L O 2012 Weibel-instability-mediated collisionless shocks in the laboratory with ultraintense lasers *Phys. Rev. Lett.* **108** 235004
[19] Emma P *et al* 2010 First lasing and operation of an ångstrom-wavelength free-electron laser *Nat. Photon.* **4** 641–7
[20] Glenzer S H and Redmer R 2009 X-ray Thomson scattering in high energy density plasmas *Rev. Mod. Phys.* **81** 1625
[21] Sperling P *et al* 2015 *Phys. Rev. Lett.* **115** 115001
[22] Fletcher L B *et al* 2015 Ultrabright x-ray laser scattering for dynamic warm dense matter physics *Nat. Photon.* **9** 274
[23] Nagler B *et al* 2015 The matter in extreme conditions instrument at the linac coherent light Source *J. Synchrotron Radiat.* **22** 520–5
[24] Gleason A *et al* 2015 Ultrafast visualization of crystallization and grain growth in shock-compressed SiO_2 *Nat. Commun.* **6** 8191
[25] Gorman M G *et al* 2015 Direct observation of melting in shock-compressed bismuth with femtosecond x-ray diffraction *Phys. Rev. Lett.* **115** 095701
[26] Amann J *et al* 2012 Demonstration of self-seeding in a hard-x-ray free-electron laser *Nat. Photon.* **6** 693–8
[27] Ciricosta O *et al* 2012 Direct measurements of the ionization potential depression in a dense plasma *Phys. Rev. Lett.* **109** 065002
[28] Albert F *et al* 2013 *Phys. Rev. Lett.* **111** 235004
[29] Zastrau U *et al* 2008 Bremsstrahlung and line spectroscopy of warm dense aluminum plasma heated by xuv free-electron-laser radiation *Phys. Rev.* E **78** 066406
[30] Nagler B *et al* 2009 Turni aren ng solid aluminium transpt by intense soft x-ray photoionization *Nat. Phys.* **5** 693
[31] Faeustlin R R *et al* 2010 Observation of ultrafast nonequilibrium collective dynamics in warm dense hydrogen *Phys. Rev. Lett.* **104** 125002
[32] Zastrau U *et al* 2014 *Phys. Rev. Lett.* **112** 105002
[33] Patel P K, Mackinnon A J, Key M H, Cowan T E, Foord M E, Allen M, Price D F, Ruhl H, Springer P T and Stephens R Isochoric heating of solid-density matter with an ultrafast proton beam *Phys. Rev. Lett.* **91** 125004
[34] Pelka A *et al* 2010 Ultrafast melting of carbon induced by intense proton beams *Phys. Rev. Lett.* **105** 265701
[35] Glenzer S H, Gregori G, Lee R W, Rogers F J, Pollaine S W and Landen O L 2003 Demonstration of spectrally resolved x-ray scattering in dense plasmas *Phys. Rev. Lett.* **90** 175002
[36] Glenzer S H *et al* 2007 Observations of plasmons in warm dense matter *Phys. Rev. Lett.* **98** 065002

[37] Gregori G *et al* 2008 X-Ray scattering measurements of radiative heating and cooling dynamics *Phys. Rev. Lett.* **101** 045003

[38] Visco A J *et al* 2012 Measurement of radiative shock properties by x-ray Thomson scattering *Phys. Rev. Lett.* **108** 145001

[39] Kritcher A L *et al* 2008 Ultrafast x-ray Thomson scattering of shock-compressed matter *Science* **322** 69

[40] Lee H J *et al* 2009 X-ray Thomson-scattering measurements of density and temperature in shock-compressed beryllium *Phys. Rev. Lett.* **102** 115001

[41] Kritcher A L *et al* 2009 Measurements of ionic structure in shock compressed lithium hydride from ultrafast x-ray Thomson scattering *Phys. Rev. Lett.* **103** 245004

[42] Neumayer P *et al* 2010 Plasmons in strongly coupled shock-compressed matter *Phys. Rev. Lett.* **105** 075003

[43] Kugland N L *et al* 2009 Evolution of elastic x-ray scattering in laser-shocked warm dense lithium *Phys. Rev.* E **80** 066406

[44] Fortmann C, Lee H J, Döppner T, Falcone R W, Kritcher A L, Landen O L and Glenzer S H 2012 Measurement of the adiabatic index in be compressed by counterpropagating shocks *Phys. Rev. Lett.* **108** 175006

[45] Regan S P *et al* 2012 Inelastic x-ray scattering from shocked liquid deuterium *Phys. Rev. Lett.* **109** 265003

[46] Ma T *et al* 2013 X-ray scattering measurements of strong ion–ion correlations in shock-compressed aluminum *Phys. Rev. Lett.* **110** 065001

[47] Zel'Dovich Y and Raizer Y 2002 *Physics of Shock Waves and High-Temperature Hydrodynamic Phenomena* ed W D Hayes and R F Probstein (New York: Dover)

[48] Drake R P 2006 *High-Energy-Density Physics: Fundamentals, Inertial Fusion, and Experimental Astrophysics* (Berlin: Springer)

[49] Frontiers in High-Energy-Density Physics: The X Games of Contemporary Science 2003 (http://nap.edu/catalog.php?record_id=10544)

[50] Betti R *et al* 2010 Thermonuclear ignition in inertial confinement fusion and comparison with magnetic confinement *Phys. Plasmas* **17** 058102

[51] Marinak M M, Kerbel G D, Gentile N A, Jones O, Munro D, Pollaine S, Dittrich T R and Haan S W 2001 *Phys. Plasmas* **8** 2275

[52] Fortov V E and Iakubov I T 2000 *The Physics of Non-Ideal Plasmas* (Singapore: World Scientific)

[53] Ichimaru S 1991 *Statistical Plasma Physics* (Reading, MA: Addison-Wesley)

[54] Hansen J P and McDonald I R 2000 *Theory of Simple Liquids* (London: Academic)

[55] Baker L M and Hollenbach R E 1972 Laser interferometer for measuring high velocities of any reflecting surface *J. Appl. Phys.* **43** 4669

[56] Geindre J P, Audebert P, Rousse A, Falliès F, Gauthier J C, Mysyrowicz A, Dos Santos A, Hamoniaux G and Antonetti A 1994 Frequency-domain interferometer for measuring the phase and amplitude of a femtosecond pulse probing a laser-produced plasma *Opt. Lett.* **23** 1997–9

[57] Fletcher L B, Galtier E, Heimann P, Lee H J, Nagler B, Welch J, Zastrau U, Hastings J B and Glenzer S H 2013 Plasmon measurements with a seeded x-ray laser *J. Instrum.* **8** C11014

[58] Gericke D O, Vorberger J, Gregori G and Wünsch K 2010 Screening of ionic cores in partially ionized plasmas within linear response *Phys. Rev.* E **81** 065401(R)

[59] Wünsch K, Vorberger J and Gericke D O 2009 Ion structure in warm dense matter: benchmarking hypernetted-chain equations by first-principle simulations *Phys. Rev.* E **79** 010201(R)

[60] Chapman D A *et al* 2015 Observation of finite-wavelength screening in high-energy-density matter *Nat. Commun.* **6** 6839

[61] Mazevet S and Zerah G 2008 *Ab initio* simulations of the *K*-edge shift along the aluminum hugoniot *Phys. Rev. Lett.* **101** 155001

[62] Vorberger J, Donko Z, Tkachenko I M and Gericke D O 2012 Dynamic ion structure factor of warm dense matter *Phys. Rev. Lett.* **109** 065002

[63] Rüter H R and Redmer R 2014 *Ab initio* simulations for the ion–ion structure factor of warm dense aluminum *Phys. Rev. Lett.* **112** 145007

[64] Clérouin J, Grégory R, Arnault P, Ticknor C, Kress J D and Collins L A 2015 Evidence for out-of-equilibrium states in warm dense matter probed by x-ray thomson scattering *Phys. Rev.* E **91** 011101

[65] Starrett C E, Daligault J and Saumon D 2015 *Phys. Rev.* E **91** 013104

[66] Souza A N, Perkins D J, Starrett C E, Saumon D and Hansen S B 2014 Predictions of x-ray scattering spectra for warm dense matter *Phys. Rev.* E **89** 023108

[67] Starrett C E and Saumon D 2015 Models of the elastic x-ray scattering feature for warm dense aluminum *Phys. Rev.* E **92** 033101

[68] White W E, Robert A and Dunne M 2015 The linac coherent light source *J. Synchrotron Radiat.* **22** 472–6

[69] Tonks L and Langmuir I 1929 Oscillations in ionized gases *Phys. Rev.* **33** 195–210

[70] Marinelli A *et al* 2015 High-intensity double-pulse x-ray free-electron laser *Nat. Commun.* **6** 6369

[71] Minitti M P *et al* 2015 Optical laser systems at the linac coherent light source *J. Synchrotron Radiat.* **22** 526–31

[72] Gamboa E J, Montgomery D S, Hall I M and Drake R P 2011 Imaging x-ray crystal spectrometer for laser-produced plasmas *J. Instrum.* **6** P04004

[73] Pak A *et al* 2004 X-ray line measurements with high efficiency Bragg crystals *Rev. Sci. Instrum.* **75** 3747

[74] Urry M K, Gregori G, Landen O L, Pak A and Glenzer S H 2006 *J Quant. Spectrosc. Radiat. Transfer.* **99** 636

[75] Zastrau U *et al* 2013 Characterization of strongly bent HAPG crystals for von-Hamos x-ray spectrographs *J. Instrum.* **8** P10006

[76] Legall H *et al* 2006 New generation of x-ray optics based on pyrolytic graphite *Proc. FEL (BESSY, Berlin, Germany)*

[77] Zastrau U *et al* 2012 Focal aberrations of large-aperture HOPG von-Hamos x-ray spectrometers *J. Instrum.* **7** P09015

[78] Dixit S N, Lawson J K, Manes K R, Powell H T and Nugent K A 1994 Kinoform phase plates for focal plane irradiance profile control *Opt. Lett.* **19** 417–9

[79] MacFarlane J J, Golovkin I E and Woodruff P R 2006 HELIOS-CR A 1D radiation-magnetohydrodynamics code with inline atomic kinetics modeling *J. Quant. Spectrosc. Radiat. Transfer* **99** 381–97

[80] Asay J R and Shahinpoor M 1993 *High-Pressure Shock Compression of Solids* (Berlin: Springer)

[81] Neal T 1979 High-pressure science and technology *AIRAP Conf. Proc.* vol 1 and 2 ed K D Timmerhaus and M S Barber (New York: Plenum)

[82] Froula D H, Glenzer S H, Luhmann N C and Sheffield J 2010 *Plasma Scattering of Electromagnetic Radiation by Sheffield* 2nd edn (New York: Academic)

[83] Gregori G, Glenzer S H, Rozmus W, Lee R W and Landen O L 2003 Theoretical model of x-ray scattering as a dense matter probe *Phys. Rev.* E **67** 026412

[84] Gregori G, Glenzer S H and Landen O L 2006 Generalized x-ray scattering cross section from nonequilibrium plasmas *Phys. Rev.* E **74** 026402

[85] Chihara J 1987 Difference in x-ray scattering between metallic and non-metallic liquids due to conduction electrons *J. Phys. F: Met. Phys.* **17** 295
[86] Johnson W R, Nilsen J and Cheng K T 2013 Resonant bound-free contributions to Thomson scattering of x-rays by warm dense matter *High Energy Density Phys.* **9** 407
[87] Fletcher L B *et al* 2014 Observations of continuum depression in warm dense matter with x-ray Thomson scattering *Phys. Rev. Lett.* **112** 145004
[88] Ichimaru S 1982 Strongly coupled plasmas—high-density classical plasmas and degenerate electron fluids *Rev. Mod. Phys.* **54** 1017
[89] Mermin N D 1970 *Phys. Rev.* B **1** 2362–3
[90] Redmer R R, Reinholz H, Röpke G, Thiele R and Höll A 2005 Theory of x-ray Thomson scattering in dense plasmas *IEEE Trans. Plasma Sci.* **33** 77
[91] Hoell A *et al* 2007 Thomson scattering from near-solid density plasmas using soft x-ray free electron lasers *High Energy Density Phys.* **3** 120
[92] Gregori G, Glenzer S H and Landen O L 2003 Strong coupling corrections in the analysis of x-ray Thomson scattering measurements *J. Phys. A: Math. Gen.* **36** 5971
[93] Fortmann C, Wierling A and Röpke G 2010 Influence of local-field corrections on Thomson scattering in collision dominated two-component plasmas *Phys. Rev.* E **81** 026405
[94] Bohm D and Pines D 1953 A collective description of electron interactions: III. Coulomb interactions in a degenerate electron gas *Phys. Rev.* **92** 609–25
[95] Zimmerman R 1987 *Many-Particle Theory of Highly Excited Semiconductors* (Leipzig: Teubner)
[96] Thiele R *et al* 2008 Plasmon resonance in warm dense matter *Phys. Rev.* E **78** 026411
[97] Döppner T *et al* 2009 Temperature measurement through detailed balance in x-ray Thomson scattering *High Energy Density Phys.* **5** 182–6
[98] Ziman J M 1961 A theory of the electrical properties of liquid metals: I. The monovalent metals *Phil. Mag.* **68** 1013–34
[99] Reinholz H, Redmer R, Röpke G and Wierling A 2000 Long-wavelength limit of the dynamical local-field factor and dynamical conductivity of a two-component plasma *Phys. Rev.* E **62** 5648
[100] Lee Y T and Moore R 1984 *Phys. Fluids* **27** 1273
[101] Fortmann C 2009 Single-particle spectral function for the classical one-component plasmas *Phys. Rev.* E **79** 16404
[102] Scopigno T, Ruocco G and Sette F 2005 Microscopic dynamics in liquid metals: the experimental point of view *Rev. Mod. Phys.* **77** 881
[103] Hansen J-P and McDonald I R 2000 *Theory of Simple Liquids* (New York: Academic)
[104] Mithen J, Daligaut J and Gregori G 2011 Extent of validity of the hydrodynamic description of ions in dense plasmas *Phys. Rev.* E **83** 015401(R)
[105] Gregori G and Gericke D O 2009 Low frequency structural dynamics of warm dense matter *Phys. Plasmas* **16** 056306
[106] Salpeter E E 1961 Energy and pressure of a zero-temperature plasma *Astrophys. J.* **134** 669
[107] Young D A, Wolford J K, Rogers F J and Holian K S 1985 Theory of the aluminum shock equation of state to 10^4 Mbar *Phys. Lett.* **108** 157–60
[108] Ross M, Yang L H and Boehler R 2004 Melting of aluminum, molybdenum, and the light actinides *Phys. Rev.* B **70** 184112
[109] Davis J-P 2006 Experimental measurement of the principal isentrope for aluminum 6061-T6 to 240 GPa *J. Appl. Phys.* **99** 103512
[110] Hau-Riege S *et al* 2012 Ultrafast transitions from solid to liquid and plasma states of graphite induced by x-ray free-electron laser pulses *Phys. Rev. Lett.* **108** 217402
[111] Fortmann C, Niemann C and Glenzer S H 2012 Theory of x-ray scattering in high-pressure electrides *Phys. Rev.* B **86** 174116
[112] Hammel B A, Haan S W, Clark D S, Edwards M J, Langer S H, Marinak M M, Patel M V, Salmonson J D and Scott H A 2010 High-mode Rayleigh–Taylor growth in NIF ignition capsules *High Energy Density Phys.* **6** 171–8
[113] Collins G W *et al* 1998 Measurements of the equation of state of deuterium at the fluid insulator-metal transition *Science* **281** 1178
[114] Gamboa E J *et al* 2015 Single-shot measurements of plasmons in compressed diamond with an x-ray laser *Phys. Plasmas* **22** 056319
[115] Yoneda H *et al* 2014 Saturable absorption of intense hard x-rays in iron *Nat. Commun.* **5** 5080
[116] Mincigrucci R *et al* 2015 Role of the ionization potential in nonequilibrium metals driven to absorption saturation *Phys. Rev.* E **92** 011101